UC Irvine

UC Irvine Electronic Theses and Dissertations

Title

CD-based Recirculation Mechanism for Liquid Manipulation and Enhanced Hybridization on Bio-microarrays

Permalink

https://escholarship.org/uc/item/9sn4p5sv

Author

Liu, Yujia

Publication Date

2022

Copyright Information

This work is made available under the terms of a Creative Commons Attribution License, availalbe at https://creativecommons.org/licenses/by/4.0/

Peer reviewed|Thesis/dissertation

eScholarship.org Powered by the California Digital Library
University of California

UNIVERSITY OF CALIFORNIA,
IRVINE

CD-based Recirculation Mechanism for Liquid Manipulation and Enhanced Hybridization on Bio-microarrays

DISSERTATION

submitted in partial satisfaction of the requirements
for the degree of

DOCTOR OF PHILOSOPHY

in Materials Science and Engineering

by

Yujia Liu

Dissertation Committee:
Professor Marc Madou, co-Chair
Professor Plamen Atanassov, co-Chair
Professor Iryna Zenyuk

2022

Portion of Chapter 1 © (2021) Royal Society of Chemistry
Portion of Chapter 2 © (2021) Royal Society of Chemistry
Portion of Chapter 4 © (2021) Royal Society of Chemistry
All other materials © 2022 Yujia Liu

TABLE OF CONTENTS

LIST OF FIGURES

LIST OF TABLES

ACKNOWLEDGEMENTS

First, I would like to express my deepest appreciation to the chair of my thesis committee, Professor Madou, for taking me under his wing and guiding me through the deep dark ocean of science. I would also like to thank my committee, Professor Plamen Anatassov, and Professor Iryna Zenyuk for their advice and guidance.

I would also like to thank my lab members, Dr. Alexandra Perebikovsky, Dr. Lawrence Kulinsky, Dr. Horacio Kido, Dian Song, Dr. Ehsan Shamloo, Dr. Maziar Ghazinejad, Dr. Sunshine Holmberg, Roya Shiri, Dr. Derosh George, Dr. Alexander Hwu, Dr. Maria Bauer, Albert Cisquella Serra, Dr. Hamsa Gowda, Alfonzo Shin, Tuo Zhou, and Jufeng Deng for their support and inspiring ideas. I would like to express my appreciations to the IMRI facility, the Rapid Tech and the laser spectroscopy labs for their incomparable devices and service. I would also like express my thanks to the companies that I've worked together with, MicrboDX, NexusDX and AMDI for their supports.

I want to thank my friends, including my two fluffy friends, Chili and Loki, for comforting and supporting me during this journey. And I want to offer my special thanks to my parents and families, who support me even we are half the earth apart. And I would like to express my deepest thanks to my wife, Qiu Qiu, who support me through my highs and lows. Without you I can never finish this journey.

I would like to acknowledge The Royal Society of Chemistry, and Springer for granting permission to incorporate some of my previously published work into my dissertation.

VITA

Yujia Liu

Education

2015 B.S. in Materials Science and Engineering, Shanghai Jiao Tong University, China

2022 Ph.D. in Materials Science and Engineering, University of California, Irvine

FIELD OF STUDY

Centrifugal microfluidics, Electrospinning, Carbon nanofibers

PUBLICATIONS

Perebikovsky, A., **Liu, Y.**, Hwu, A., Kido, H., Shamloo, E., Song, D., ... & Madou, M. (2021). Rapid sample preparation for detection of antibiotic resistance on a microfluidic disc platform. *Lab on a Chip*, *21*(3), 534-545.

Hui, Y., **Liu, Y.**, Tang, W. C., Song, D., Madou, M., Xia, S., & Wu, T. (2019). Determination of mercury (II) on a centrifugal microfluidic device using ionic liquid dispersive liquid– liquid microextraction. *Micromachines*, *10*(8), 523.

Liu, Y., Lau, E., Mager, D., Madou, M. J., & Ghazinejad, M. (2021). Distinct Roles of Tensile and Compressive Stresses in Graphitizing and Properties of CarbonN anofibers. *Micromachines*, *12*(9), 1096.

Ghazinejad, M., **Liu, Y.**, Lau, E., Madou, M., & Mager, D. (2021, August). Tuning microstructure and characteristics of carbon nanofibers by stress-induced graphitization. In *Low-Dimensional Materials and Devices 2021* (Vol. 11800, p. 1180003). International Society for Optics and Photonics.

Liu, Y., Kulinsky, L., Shiri, R., & Madou, M.J.(2021) Elastic membrane enabled inward pumping for liquid manipulation on a centrifugal microfluidic platform. Under preparation

Patents

Perebikovsky, A., Churchill, B., Churchman, S., Haake, D. A., Halford, C. W., **Liu, Y.**, ... & Monti, G. (2020). *U.S. Patent Application No. 16/641,793*.

Madou, M., Perebikovsky, A., **Liu, Y.**, Kido, H., Churchman, S. A., & Halford, C. W. (2021). *U.S. Patent Application No. 17/054,306*.

Monti, G., Halford, C. W., Perebikovsky, A., **Liu, Y**., Kido, H., Haake, D. A., ... & Churchill, B. (2020). *U.S. Patent Application No. 16/636,259*.

ABSTRACT OF THE DISSERTATION

Centrifugal Microfluidic Platform for Antibiotic Susceptibility Test and Recirculation Mechanism for Liquid Manipulation on CD

by

Yujia Liu

Doctor of Philosophy in Materials Science and Engineering

University of California, Irvine, 2022

Professor Marc Madou, co-Chair

Plamen Atanassov, co-Chair

Infectious diseases have been notorious killers since the beginning of human history. As antibiotics were discovered to efficiently treat infectious diseases, they also cause antibiotic resistivity in bacteria. It could result in huge death tolls and economic losses if not being handled properly. As a potential tool to address these crises, centrifugal microfluidic platforms have been widely investigated for decades. In this work, we demonstrated the development of a centrifugal microfluidic platform for sample preparation of assays, including liquid manipulation via laser valves, cell lysis of gram-positive and gram-negative bacteria, and incubation of bacteria from different species. We also presented a novel recirculation mechanism for inward pumping, mixing, and hybridization enhancement. The mechanism was studied parametrically and theoretically to provide practical design guidelines. A recirculation integrated blood/plasma separation design was tested as a potential application. A preliminary study was carried out to show its potential in assay hybridization. Finally, we designed and fabricated a centrifugal disc, and used the platform we developed to implement a phenotypic antibiotic susceptibility test that successfully identifies antibiotic resistance against 5 types of antibiotics among 11 different species of *E. Coli* in 2 hours.

Chapter 1

Introduction and Background

1.1 Introduction

Infectious diseases have been living among us since prehistoric times, greatly affecting both human history and biology [1]. As human societies shifted from hunter-gatherers to agricultural societies, there are more and more emerging infectious diseases that originated from wild animals and livestock [2]. In the past two centuries, rapid globalization accelerated the emergence of new infectious diseases, facilitating their spread from continent to continent and causing huge economic loss and enormous death toll [3]. Since the beginning of this century, outbreaks, epidemics, and pandemics such as severe acute respiratory syndrome (SARS), H1N1 influenza, cholera, H5N1 influenza, and Ebola virus disease (EVD), occur more frequently, which greatly affected human health and life quality. The most recent outbreak, coronavirus disease 2019(COVID-19) had escalated into a global pandemic that greatly shook the world. By the end of 2021, it has taken over 5 million lives and economic loss in trillions of dollars [4].

The crisis of infectious diseases not only lies in the containment of spread but also the use of medicines as the drug resistivity builds up over time. The pathogens that cause infectious diseases are prominently viruses, such as influenza and COVID-19, and bacteria, such as cholera. For bacterial infections, the treatment plan usually involves the use of antibiotics [5–7]. Since their discoveries, antibiotics have saved countless lives and are still

being used daily for severe infections and critical surgeries. However, the abuse of antibiotics has led to the emerging crisis of antimicrobial resistance. Moreover, the low profit and long developing time of new types of antibiotics have led to a discovery void since 1987 [7,8]. Since then, few novel antibiotic classes are under development. With fewer and fewer available antibiotics, a post-antibiotic era will come inevitably. According to a report by the UK government, there are 25,000 people die each year as a result of hospital infections caused by resistant bacteria in Europe. If we fail to control the development of antibiotic resistance, resistant bacterial infections could result in 10 million deaths by 2050 and economic losses in trillions of pounds [9].

To address these health crises, a critical step is providing accessible diagnosis tools for patients at the early stage of the infections. After the SARS outbreak, the WHO adopted the new International Health Regulations (2005) in 2007, which urges the member states to evaluate and enhance their capabilities of detecting and assessing any potential health crisis at the primary public health response level [10]. However, such diagnostic tests often require well-equipped laboratories, professional staffs, and well-established infrastructure, which is impractical to be practiced by small clinics that are accessible to most of the patients. For example, the current practices of antibiotic susceptibility tests (ASTs) are culture-based approaches that usually involve two steps of incubation of the specimen [11,12]. The first incubation step allows the physician to confirm the presence and the type of bacteria by observing the formation of bacteria colonies. Then a second incubation step with specific antibiotics is performed to determine the antibiotic susceptibility of the bacteria. Both of these two incubation steps are time-consuming and labor-intensive,

making the entire AST procedure not suitable to be deployed at the primary health care level.

The concept of point of care (POC) diagnosis was brought up by researchers who are seeking solutions to make diagnostic tests more available for patients. It visualizes a type of miniaturized diagnostic tool that can provide onsite tests with high sensitivity and specificity. Additionally, these tools should have a simple sample collection step, high level of automation, on-board reagent storage, robustness in a resource-limited environment, and easy interpretation of the results. To ensure that the tools are practical and deployable in rural areas and developing countries, the costs, and scalabilities should also be considered. In 2006, the WHO put forward the "ASSURED" criteria: Affordable, Sensitive, Specific, User-friendly, Rapid and robust, Equipment-free, and Deliverable to end-users for diagnostic tests targeting sex transmitted diseases [13]. It later became the benchmark for the development of POC diagnostic tools.

Figure 1.1. The “ASSURED” criteria from WHO: Affordable, Sensitive, Specific, User-friendly, Rapid and robust, Equipment-free, and Deliverable to end-users [13].

Efforts have been made in various related fields to develop diagnostic tools that meet these requirements. With the advances in microbiology, molecular biology, and nanomaterials, genotypic ASTs that use nuclei acid amplification methods such as polymerase chain reaction (PCR) and loop-mediated isothermal amplification (LAMP), have been successfully developed in laboratory settings. These approaches can identify specific known genes that provide antibiotic resistance, therefore bypassing the lengthy incubation steps and can be performed in minutes. However, they have either a high false-positive rate caused by the resistant non-pathogenic bacteria from the patient specimens or a high false-negative rate, as unknown resistant genes are undetectable by these methods [14,15]. Therefore, the results from genotypic ASTs still need to be validated by phenotypic tests, which makes the challenge of the lengthy and labor-intensive bacteria incubation inevitable.

The progress in microfluidics has provided different approaches to facilitate the incubation step of phenotypic ASTs. One strategy is trapping individual bacterium cells using microfluidic confinement, antibody capture, or agarose encapsulation [16]. As the confined space accelerate the incubation by shortening the diffusion distance of antibiotics and making it easier to track the behavior of individual cells, the growth of the cells can be observed by high-resolution microscope imaging, fluorescent imaging, gram staining, or analyzing the metabolite production of intracellular fluid [17–21]. However, these methods have limitations respectively, with either expensive time-lapse imaging microscope with hours of observation, labor-intensive characterization assays, or limited types of bacteria that can be studied[22,23]. Furthermore, the separation of individual cells may neglect the interaction between cells during incubation with antibiotics in a polymicrobial sample [24].

Figure 1.2. The SpinBox design and components.

In this thesis, we presented a portable sample-to-answer centrifugal microfluidic system (SpinBox) as shown in Figure 1.2, which automates the assay steps of nuclei acid-based phenotypic ASTs. With a specifically designed cartridge, the system is capable of conducting assay steps of phenotypic AST, including but not limited to bacteria incubation, bacteria lysis, liquid mixing, nuclei acid/protein probe hybridization, washing, and detection. To address the incubation challenge, we developed a novel on-disc incubation that uses the rRNA of bacteria as the growth indicator. A bacterial lysis technique was also implemented on the system to extract the rRNA from both gram-positive and gram-negative bacteria. To provide precision valving, we deployed a laser valving technique with reliability and robustness. We also invented a recirculation mechanism that can be used as an inward pumping mechanism and hybridization enhancing technique. In the end, we demonstrated the implementation of a phenotypic AST with 11 different bacteria isolates

and 5 types of antibiotics using this system, showing its capability of diagnosing antibiotic susceptibility in 2 hours.

1.2 Centrifugal microfluidics

In the past few decades, lab-on-a-chip (LoC) systems have been intensively investigated as platforms for analytical and biological chemistry. With key features including low costs, consistency, time and labor-saving, small sample volume required, portability, and programmability, LoC systems are believed to have great potential for different application areas in biotechnology, diagnostics, medical, pharmaceutical or environmental industries [25,26]. As a subcategory under the lab-on-chip (LoC) system, the centrifugal microfluidic platform, which is also called the lab-on-disc (LoD) system, inherited the appealing features from its parent. More attractively, a centrifugal field generated by a rotary motor is applied across entire the disc shape cartridge, providing three pseudo forces: centrifugal force, Euler force, and Coriolis force as shown in Figure 1.3. With various forms of valves, cartridge designs, and spinning protocols, these forces can conduct basic fluidic manipulations on a centrifugal disc (CD), such as aliquoting, pumping, valving, mixing, removal of bubbles, and separation based on density[27–29]. Compared to traditional LoC systems, the simplicity of fluidic control in LoD systems eliminates the use of bulky and expensive pumping systems [30]. Meanwhile, the rotational symmetry of the disc enables the multiplexing of tests on one cartridge, highly increasing the throughput of the devices [29,31,32].

Apart from the intrinsic advantages of the rotational nature, centrifugal microfluidic platforms have also been equipped with off-disc active components that enable various

functions. Implemented with heating and cooling element, camera, lenses, and excitation LEDs, the centrifugal microfluidic platform can perform the basic functions of PCR thermocycler, benchtop incubator, cell separator, droplet generator, cell lyser, centrifuge, microscope, and vortex mixer with only a small fraction of the price [33]. The low cost and versatility of centrifugal microfluidic systems are favorable for commercialization, as the same device can perform various biological assays with little modifications on the test cartridges. As a result, CD devices have been successfully commercialized for POC diagnostics, as some examples are shown in Figure 1.4.

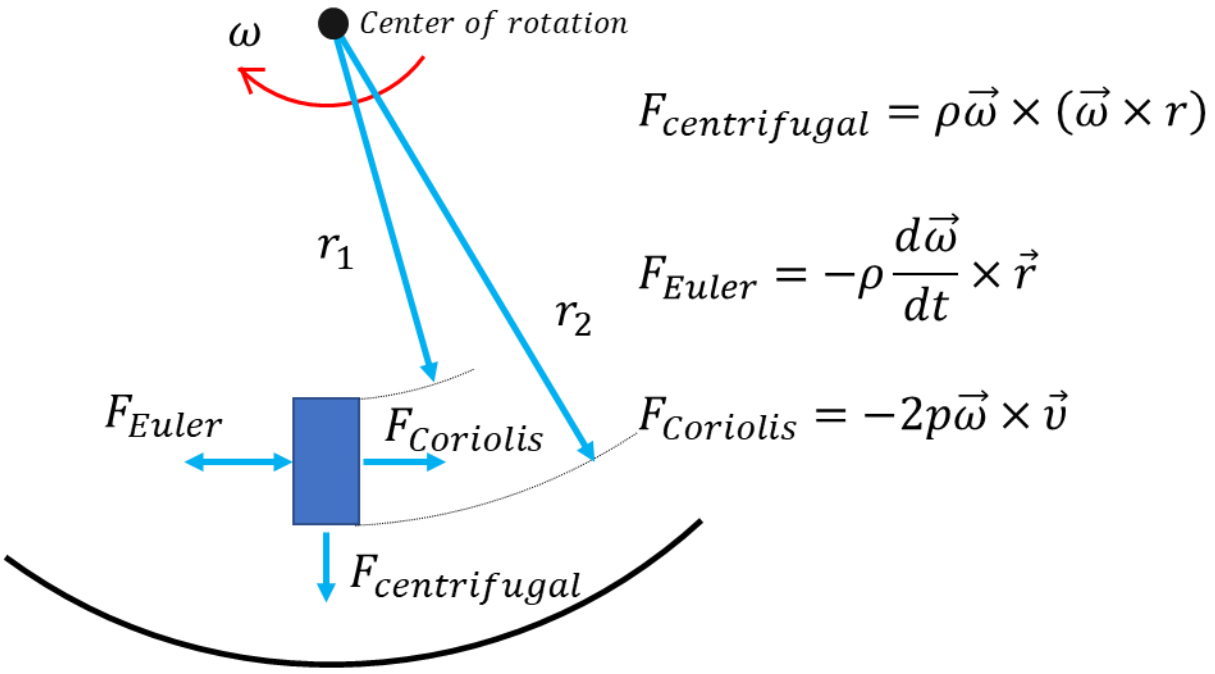

Figure 1.3. The three pseudo forces that generated by the rotation of the disc: the centrifugal force, the Euler force, and the Coriolis force.

Figure 1.4. Examples of commercialized CD products for POC diagnostics. a) Piccolo XPRESS from Abbott (CA, USA) [34]. b) Nexus IB10 from NexusDx (CA, USA) [35]. c) Revogene from Meridian Bioscience (OH, USA) [36]. d) WaterLink Spin Touch from LaMotte (MD, USA) [37]. e) Rhonda from Spindiag (Freiburg, Germany) [38]. f) Gyrolab xPlore from Gyros Protein Technologies (Uppsala, Sweden) [39].

1.3 Liquid manipulation mechanisms on CD

To manipulate fluids on the CD, it is important to understand the physics on the rotary platform. As mentioned in the previous section, centrifugal microfluidic platforms primarily use the three inherent pseudo forces generated by the rotary motor: the centrifugal force, the Euler force, and the Coriolis force. They can be described by the following equations:

$$\vec{F}_{total} = \vec{F}_{centrifugal} + \vec{F}_{Eular} + \vec{F}_{Coriolis} \quad \text{(Eq 1.1)}$$

$$\vec{F}_{centrifugal} = \rho\vec{\omega} \times (\vec{\omega} \times r) \quad \text{(Eq 1.2)}$$

$$\vec{F}_{Eular} = -\rho \frac{d\vec{\omega}}{dt} \times \vec{r} \quad \text{(Eq 1.3)}$$

$$\vec{F}_{Coriolis} = -2p\vec{\omega} \times \vec{v} \quad \text{(Eq 1.4)}$$

where ρ is the liquid density, $\vec{r}$ is the average distance of liquid front the rotation center, $\vec{\omega}$ is the angular velocity, and $\vec{v}$ is the velocity of the object moving on the CD. As the centrifugal force can be easily controlled by the angular velocity of the CD, it is used as the main pumping force to drive liquid on the disc. The Euler force depends on the angular acceleration of the CD and has a direction perpendicular to the centrifugal force. Therefore, it is usually used for fluid mixing. As the Coriolis force has a direction perpendicular to the velocity of the fluid object and opposite to the angular velocity of the disc, it can be used as a separation tool in flow-switching techniques [40,41]. It is important to note that the net force of the three pseudo forces generally points radially outwards, highly limiting the freedom to manipulate liquid on CDs. Therefore, additional valving and pumping mechanisms are required to obtain precision fluidic control.

1.3.1 Valving

Basic valving mechanisms on the LoD systems can be categorized into passive valves and active valves depending on the use of external actuation mechanisms. There are mainly three types of passive valves: capillary valve, hydrophobic valve, and siphon valve, as shown in Figure 1.5. The capillary valve stops the liquid by balancing the centrifugally induced pressure, with the capillary pressure at the liquid-air interface near the abrupt broadening section of the hydrophilic capillary channel. As the angular velocity of the CD increases to a critical value, the capillary valve will burst to allow the liquid flow, and this critical value is called burst velocity. Capillary valves have been widely used for fundamental fluidic controls, however, have limitations such as the number of valves is

highly restricted by the motor capability, and the burst velocity is highly affected by manufacture defects [27,28,42]. Similar to the capillary valve, the hydrophobic valve balances the pressure generated by the centrifugal force and the capillary pressure generated by a hydrophobic patch. Like capillary valves, these valves face similar limitations. The siphon valve can hold the liquid under a high angular velocity of the CD as the meniscus front in the siphon stays radially outer than (or below) the crest. As CD slows down, the capillary force in the siphon drives the liquid over the crest and primes the siphon. The valve is then opened by simply increasing the angular velocity of the CD, as the hydrostatic pressure difference will drain the liquid in the original chamber [43]. Despite the simplicity and robustness of the siphon valve, it often requires localized hydrophilic treatment of the siphon, which imposes challenges in CD fabrication and could deteriorate within weeks [42,44].

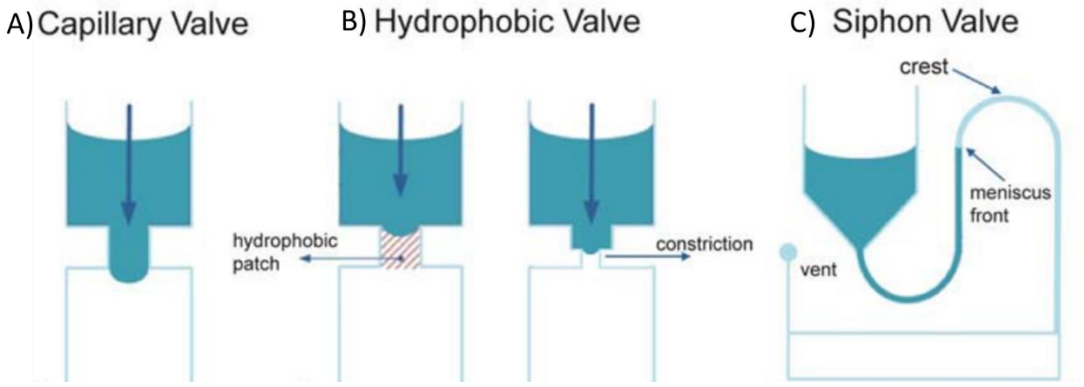

Figure 1.5. Different types of passive valves. a) Capillary valve. b) Hydrophobic valve. c) Siphon valve. Reprinted from [45].

Recent progress on pneumatic valving has provided more tools to manipulate fluid on a CD. Gorkin et al. reported a mechanism that uses a pneumatic chamber for siphon valving as shown in Figure 1.6 [46]. At the initial state, all liquid rest in the loading chamber. As the

angular velocity of CD increases, the liquid is transported into a ventless chamber and the air is compressed. The liquid remains in this very chamber until the angular velocity decreases to a certain value that the liquid must fill the siphon to balance the pneumatic pressure in the ventless chamber. Upon the priming of the siphon, liquid can be transported into the receiving chamber and the valving process is completed. Another passive valving mechanism called the timed valving mechanism was reported by Schwemmer et al. [47]. It interplays the pneumatic energy between two pneumatic chambers which were connected with a high resistance timing channel. By changing the viscous dissipation in the timing channel, this valving mechanism can control the release of pneumatic energy in the second chamber to achieve timed valving. However, an inevitable disadvantage of these passive valves is that they are not vapor-tight, which may cause contamination and deterioration of the stored reagent.

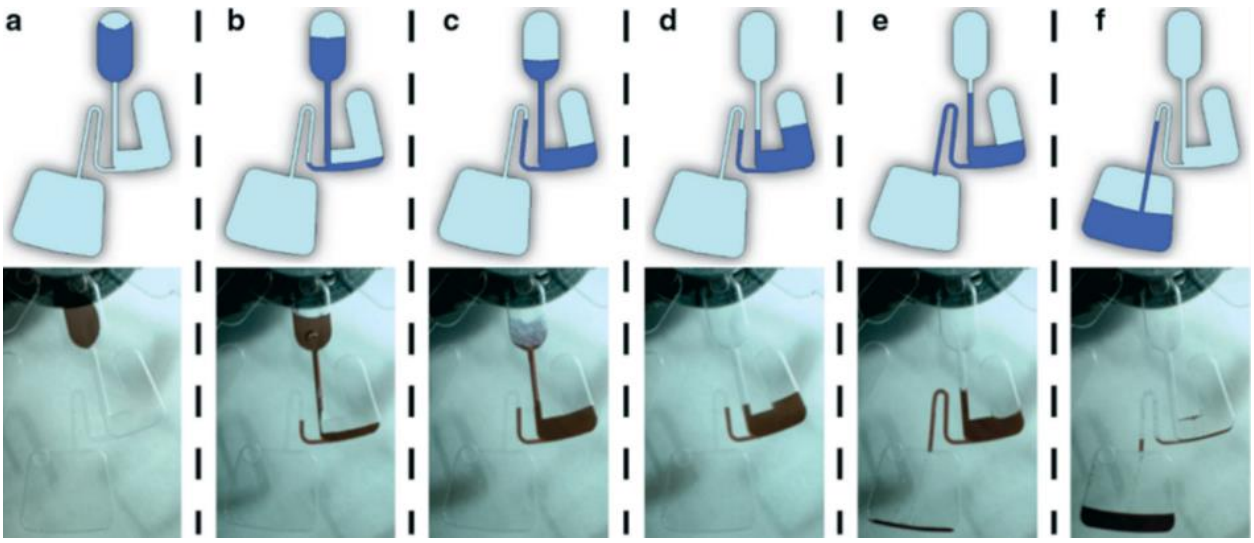

Figure 1.6. Pneumatic siphon valving mechanism that uses a ventless chamber to prime a siphon. Reprinted from [46].

Considering the limitations mentioned above, researchers turned to active components for more reliable and robust valving mechanisms. Sacrificial valves use different types of sacrificial materials that can be destroyed under certain conditions such as laser or heat. For example, the use of wax allows the normally closed channel to be opened or vice versa under an external heat source [48,49]. Driver-controlled reversible diaphragm valves are reported by Kim et al., which uses a screw driver to push a diaphragm that blocks the channel[50]. This screw-block approach has been further improved by Aeinehvand et al. by turning a screw in the valve seat to adjust the sealing pressure [51].

Besides the two basic valving types mentioned above, there are other types of valving mechanisms that have been developed with attractive features. Among them, biocompatible dissolvable film valves have been well researched. As shown in Figure 1.7, with a pneumatic chamber to prevent airflow at the low angular velocity, the dissolvable film valve remains intact. As the CD accelerated to a certain angular speed, gas/liquid inversion occurs, and the valve is dissolved [52].

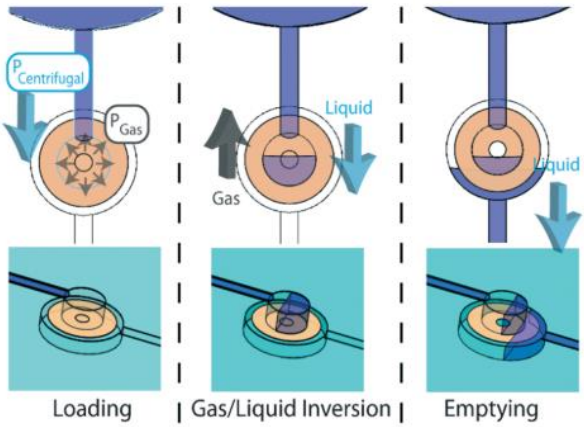

Figure 1.7. Dissolvable film valve. With a pneumatic chamber to prevent airflow at the low angular velocity, the dissolvable film valve remains intact. As the CD accelerated to a certain angular speed, gas/liquid inversion occurs, and the valve is dissolved. Adapted from [52].

1.3.2 Pumping

Since the outwards pumping can be easily achieved by the centrifugal force alone, the interest in developing novel pumping mechanisms primarily focuses on the inward pumping mechanism. Like valving mechanisms, pumping mechanisms can also be categorized as active pumping and passive pumping, depending on the use of any external power source. Active pumping mechanisms use external components to apply thermal, mechanical, or electrical energy that drives the liquid on the disc inwards. For example, Abi-Samra et al. developed a thermal-pneumatic pumping mechanism where the air in a ventless chamber expands under heating to pump liquid back to the center during spinning[53]. Another assisted pneumatic pumping mechanism was developed by Kong et al., providing an inward pumping force by applying externally pressurized air through an opening on the CD[54]. In 2015, a mechanical inward pumping mechanism was achieved using a fly ball system, which acts on a chamber with a deformable polymer membrane in a direction perpendicular to the rotation plane, pushing the liquid in the same chamber inwards during spinning[55]. With the introduction of electricity on a CD through either inductive coils or slip-rings, various electrical pumping mechanisms have been developed[56,57]. Electrolysis generating gas inside a ventless chamber can pump liquid inward with a similar disc configuration as in thermal-pneumatic pumping[56,58]. Direct pumping liquid back to the center has also been achieved by mounting electronic pumps directly on the disc[46,57].

The passive-pumping mechanism, as its name implies, does not require external components to provide energy for pumping the liquid back to the disc center. Various disc

configurations and spinning protocols have been demonstrated to achieve inward pumping. One of the simplest mechanisms relies on capillary force to bring liquid back to the center of the CD by using hydrophilic materials, allowing a portion of the liquid to flow back to its original chamber[59]. Pishbin et al. developed a mechanism that uses Euler force generated by abrupt deceleration of the spinning disc from 2500 rpm to 50 rpm. This way, liquid can be pumped to a chamber closer to the center of the disc through a guiding channel[60]. However, the requirement of surface treatment and a strong motor, as well as the low pumping efficiency, limit the implementation of this method in a practical assay. To achieve comparably higher pumping efficiencies, displacement pumping mechanisms were developed by using displacer liquids to pump target liquid inward[61,62]. However, despite the higher efficiency, the sophisticated displacement mechanism requires too precise a coordination among chambers and preloaded liquids. Another high-efficiency pumping mechanism, dynamic-pneumatic pumping based on compressing air in a ventless rigid chamber, was reported by different groups[45,63,64]. As shown in Figure 1.8, the liquid initially is loaded in the inlet chamber. As the CD spins at a high angular velocity, the air in the compression chamber is compressed by the liquid. With an abrupt deceleration, liquid flows inwards through both the inlet channel and outlet channel under the pneumatic pressure in the compression chamber. As the liquid flows faster in the outlet channel which has distinctively smaller fluidical resistance, most of the liquid is pumped inward to the collection chamber. These mechanisms were further improved by Aeinehvand et al. by replacing a rigid chamber with a latex micro-balloon to decrease the operation spin speed and increase the pumping volume[56,65,66].

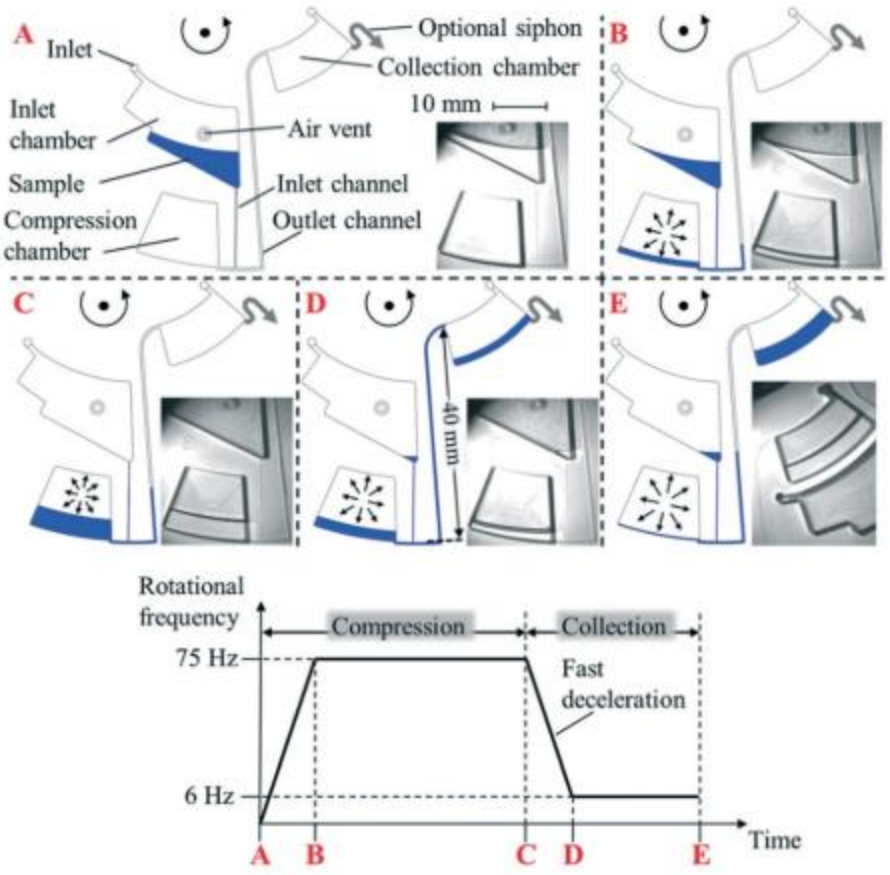

Figure 1.8. Passive pneumatic inward pumping. a) The liquid initially is loaded in the inlet chamber. b), c) As the CD spins at a high angular velocity, the air in the compression chamber is compressed by the liquid. d) With an abrupt deceleration, liquid flows inwards through both the inlet channel and outlet channel under the pneumatic pressure in the compression chamber. e) As the liquid flows faster in the outlet channel which has distinctively smaller fluidical resistance, most of the liquid is pumped inward to the collection chamber. [63]

1.4 CD as a multifunctional platform

With the help of different valving and pumping mechanisms, various basic laboratory operations have been achieved on a CD platform. One of the fundamental operations is pipetting to measure and transfer the appropriate volume of liquid. This has been achieved by using an overflow channel connected to a chamber with a specific volume[28,45]. Once

the liquid level reaches the overflow channel, additional liquid is removed through this channel to a waste chamber.

Another essential operation for biological assays is the mixing process to facilitate the reaction process and obtain a homogenous solution. It is especially important in the microfluidic domain as the low-Reynolds number inhibits the convection through turbulence flow and only the slow diffusive mixing is allowed[67]. However, for LoD systems, liquid usually flows into large chambers on CDs, allowing the mixing through both diffusion and convection. The flow inertia can further facilitate the convective mixing by the rapid oscillation of the CD [28,45]. Additional methods have also been developed to mix liquid when a small chamber or confined space is needed. Ducree et al. showed that the mixing can be achieved by Coriolis force during the continuous flow in chambers and channel, which is further simulated by La et al. and optimized by Kuo et al. [29,68,69]. Bubble promoted mixing has also been achieved on CD by chemical decomposition of gas generating reagent (such as H_2O_2) and heating of a ventless air chamber [70,71]. Noroozi et al. developed a flow reciprocation mechanism that utilizes the centrifugal force and a pneumatic pressure from a ventless chamber, which allows liquid mixing in a confined space without the generation of bubbles or the need for a long channel [72]. It was further adopted as a hybridization strategy for immunoassays, significantly shortening the assay time [73]. Magnetic mixing has also been reported by mixing chemically inert magnetic components in the liquid. Under the external magnetic field, the magnetic components create chaotic advection to facilitate mixing [74]. This technique has also been used to create intense mixing for the lysis of cells, which releases genomic data for nuclei acid analysis [75]. Such lysis method is discussed in this thesis with parameter optimization.

Taking the advantage of the centrifugal force, the CD platform can perform heterogeneous mixture separation as a centrifuge based on the density difference of the components. One of its important applications is blood/plasma separation, which is often operated by a technician using a centrifuge and the supernatant is collected with a pipette. By spinning the CD at a high angular velocity, blood cells are sedimented at the bottom of the chamber. The supernatant is then collected in a collection chamber by an overflow channel or a siphon [76,77]. However, to obtain a high separation efficiency and a short separation time, the blood/plasma separation usually requires a large radius and high spin speed of the cartridge. Therefore, this function unit is usually placed at the edge of a CD. To utilize the real estate of the full radius, we developed an inward pumping mechanism that transfers the plasma to the center of the CD, which will be discussed in later sections.

Apart from the basic laboratory operations mentioned above, the CD platform has been equipped with axillary components to fulfill various functions. Microorganisms cultivation and monitoring have been achieved with *Caenorhabditis elegans* and *Pichia pastoris* [78,79]. We also developed a universal bacteria incubation system that can be used for antimicrobial susceptibility observation, which will be detailly described in the next chapter [80].

The detection of biomolecules has also been achieved on centrifugal microfluidic platforms. For sensitive and specific detection of pathogens like bacteria and viruses, nucleic acid amplification methods such as PCR and LAMP have been successfully implemented [81–87]. It is noteworthy that quantitative nucleic acid amplification techniques using digital droplet methods have also been achieved via different approaches, providing detection

methods for biomedical diagnosis and environmental monitoring at a low level of pathogen concentration [88–91]. As a standard method in medical practice for diagnosis and vaccination validation, the detection of pathogen-related protein has been developed into rapid diagnostic kits. In a laboratory setting, the detection of protein is usually conducted via enzyme-linked immunosorbent assay (ELISA), which requires long probe hybridization and labor-intensive pipetting. The CD platforms are developed to facilitate the reaction and shorten the assay time by the short diffusion distance in the microfluidic domain and advection-assisted transport through mixing mechanisms [92,93]. Kim et al. developed a CD immunosensors based on electrochemical detection [94]. As shown in Figure 1.9, with a slip ring that provides power on the CD, the electrochemical assay can be performed during spinning. Other detection methods for proteins such as fluorescent immunoassays and lateral flow strip sensors are also investigated, with commercial products available [35,73,95].

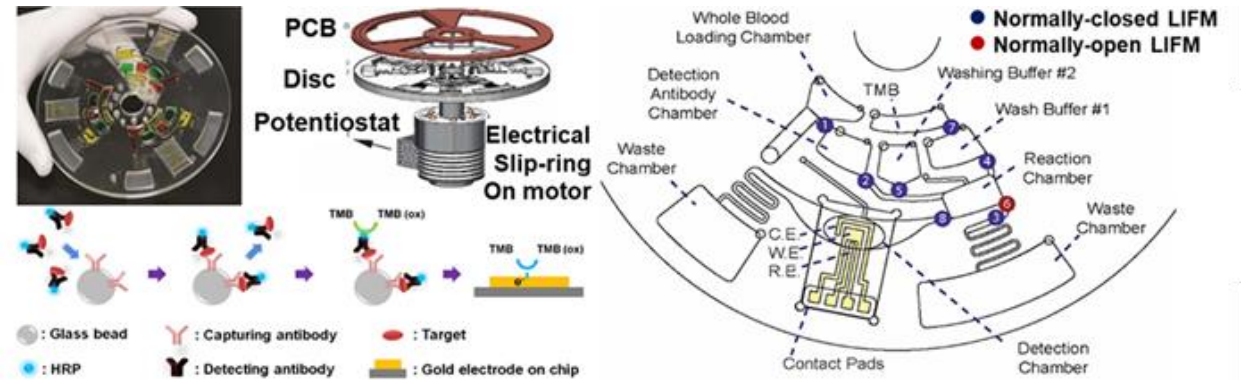

Figure 1.9. Slipring enabled on-disc electrochemical immunoassay. Reprinted from [94]

To summarize, the progress in CD platforms has demonstrated their capabilities of carrying out various functions of different biological assays. Its versatility also makes it more

attractive as an ideal platform for POC applications. In the next chapter, we will demonstrate how we build a portable centrifugal microfluidic platform. We will also validate its functionalities by implementing the steps from a bacteria-related assay, including basic fluidic manipulation, incubation, cell lysis, and optical detection.

Chapter 2

Design and Fabrication of Centrifugal Microfluidic System

In this chapter, we described the design, fabrication of the centrifugal microfluidic system, and function validation based on a phenotypic antibiotic susceptibility test.

2.1 Material and method

2.1.1 Instrument fabrication

The instrument of the centrifugal microfluidic platform conducts biological assays on CDs. It is primarily built from off-the-shelf material and 3D-printed parts. The instrument fabrication can be divided into several units, including the instrument-cartridge interface, laser valving unit, optical unit, thermal control unit, program control unit, and the enclosure.

For the instrument-cartridge interface, we used a custom machined spinchuck (Appendix A Figure A1c and two spring-loaded balls to hold the CD with tight tolerance. The spinchuck was secured on the shaft of the main motor (Anaheim Automation Inc., CA, USA), which is controlled by a motor controller (AllMotion, CA, USA). We used a linear actuator (Actuonix, BC, Canada) to move a laser diode. By coordinating with the main motor, the laser can be located at any position on the CD. An optical unit was designed to conduct fluorescence detection using a Mako G-507B CMOS camera (Allied vision, German), an excitation LED (Thorlabs, NJ, USA), and a set of filters and dichroic beamsplitter (Thorlabs, NJ, USA). To accommodate different CD designs, an adjustable camera mount was used to manually

focus the camera onto the detection area. To maintain the temperature during incubation, we fabricated a customized heater using nichrome wires (McMaster Carr, CA, USA) as the heating element and mica sheets (McMaster Carr, CA, USA) as the heat shielding material to protect other components. A fan is constantly blowing through the U shape heater housing to circulate air in the test chamber. To control the temperature, a PID controller was used to control the current that goes through the heating wires.

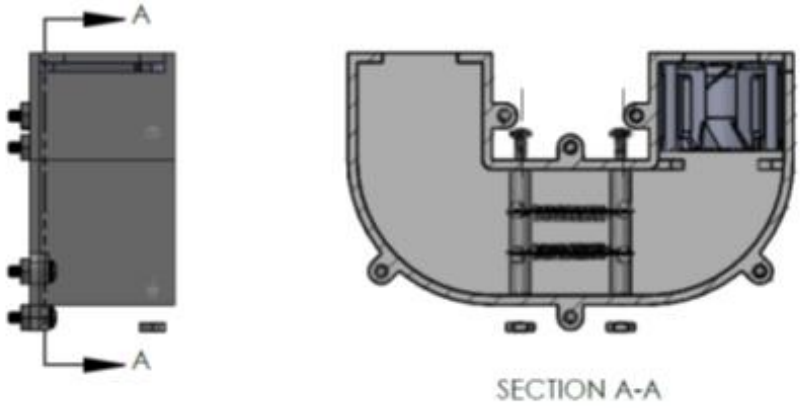

Figure 2.1. The customized heater uses a 3D printed housing to encapsulate nichrome wires as the heating coils and mica sheets as the heat shielding material to protect other components. A fan is constantly blowing towards the wire to circulate air in the test chamber.

For the controlling system, we used a Raspberry Pi 3B+ running NOOBS operation system. A 7-inch touchscreen was used to enable easy user interaction. The controlling program was written in Python3 with a user-friendly interface (shown in Appendix A), which is available at [96]. An algorithm was used to process the image using the OpenCV library. A prototyped PCB was used to distribute power and control other units. The enclosure of the instrument was assembled from PMMA (McMaster Carr, CA, USA), 3D printed components, and t-slot extrusions (McMaster Carr, CA, USA), which is described in Appendix A.

2.1.2 Microfluidic disc fabrication

Four different types of microfluidic discs were fabricated in this work: prototype cyclic olefin copolymer (COC, TOPAS) discs manufactured using a CNC machine at microfluidic Chipshop GmbH (Jena, Germany), cyclic olefin copolymer (COC, TOPAS) injection molded discs obtained from microfluidic Chipshop GmbH (Jena, Germany), and prototype poly(methylmethacrylate) (PMMA) discs fabricated using a laser cutter (Trotec Speedy 360). CDs were designed in SolidWorks (Dassault Systèmes SOLIDWORKS Corp.) and assembled using different strategies.

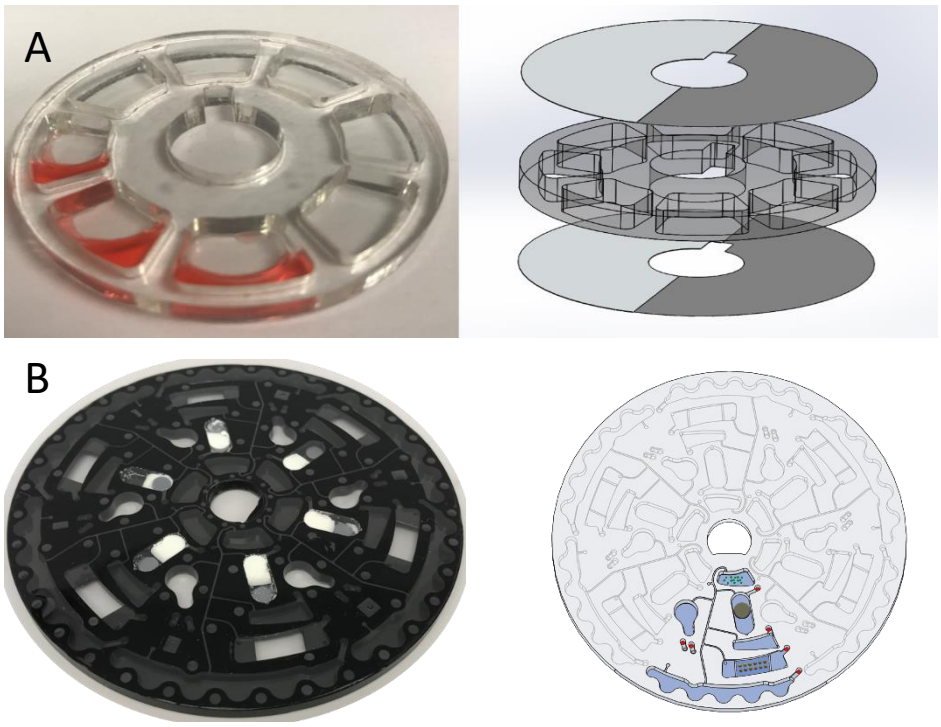

Figure 2.2. The CD design and assembly diagram for a) incubation test and b) lysis efficiency test. For the lysis test, the discs are preloaded with sodium hydroxide, metal discs, and silica-zirconia beads in the lysis chamber.

For incubation tests, we used the laser-cut PMMA disc covered by gas-permeable, single-sided adhesives (MP Biomedicals 097640205) with a design shown in Figure 2.2a. For the

lysis test, the disc design is shown in Figure 2.2b, which is prototyped by CNC machining of COC material and then manufactured by injection molding. This design that features laser valves was also used for the automation of antibiotic susceptibility tests. NaOH was stored in a groove machined in the center of the lysis chamber and sealed using wax. A metal disc that facilitates cell lysis was placed on top of the wax seal to prevent the premature release of NaOH. Equal quantities of lysis beads were dispensed into the lysis chambers using a slurry of silica-zirconia beads mixed with polyvinyl alcohol. The disc was then placed into a vacuum heater at 40 °C for 30 minutes. Dried down phosphate buffer (1X) and detector probes were dispensed into the neutralization chamber prior to assembly. Finally, the COC inner feature layer was placed on an alignment jig and sandwiched between two transparent, gas-permeable, single-sided adhesives (MP Biomedicals 097640205) that were cut to shape using a polyvinyl cutter (Silhouette Cameo 2). A double-sided adhesive (3M 300 LSE) was affixed to the cutout on the bottom of the detection chamber of the disc, creating a fluidic seal between an optional, modular microarray and the detection chamber of the disc.

2.1.3 Bacteria, antibiotics, and media

E. coli clinical urine isolates were obtained from the University of California, Los Angeles (UCLA) Clinical Microbiology Laboratory with approval from the UCLA and Veterans Affairs Institutional Review Boards and appropriate Health Insurance Portability and Accountability Act exemptions. Bacteria were inoculated into Mueller-Hinton (MH) broth with 12% glycerol (Becton, Dickinson, Sparks, MD) and stored at -80 °C.

Experiments were conducted from the frozen isolates. Bacteria were defrosted and cultured overnight by inoculating 5 mL of freezer stock bacteria into 5 mL of cation-adjusted Mueller Hinton (MH2) broth (Sigma, St. Louis, MO) and incubating in a shaker incubator at 37 °C. The following day, working samples were prepared by diluting the overnight culture with MH2 broth to ~6×10^5 cfu/mL. The prepared cultures were pipetted into the incubation chamber on the disc or 96-well plate and immediately sealed. Bacteria were also plated on LB agar (MOBIO Laboratories Inc., Carlsbad, CA) to verify the colony forming units (cfu).

For rapid incubation experiments, either 75 mL or 200 mL of prepared cultures were pipetted into each chamber of the disc or 96-well plate and placed in the appropriate spinstand incubator or shaker incubator. Bacteria were incubated at 37 °C and oscillated at 1 Hz through an angle of 180 on the spinstand or 400 rpm on the tabletop shaker. The sample was collected for plating or lysed for Luminex analysis at different timestamps, 0 min, 60 mins, and 90 mins to be specific. Serial dilutions (10^{-6}) were performed prior to triplicate plating and were incubated overnight prior to counting the following day. For Luminex readings, 70 mL of sample was removed from the chambers and mixed with 35 mL of 1M NaOH for 5 minutes. The sample was neutralized by adding 105 mL of phosphate buffer solution. 150 mL of neutralized lysate was collected and characterized using a Luminex MagPix assay instrument with custom capture probes designed to hybridize with oligonucleotides on Luminex MagPlex-TAG microspheres (Luminex, TX, USA).

In certain growth experiments, cultures were spiked with one of the following antibiotics diluted in (MH2) broth before incubation in the disc: 4 mg/ml ciprofloxacin (Sigma, St.

Louis, MO), 32 mg/ml ceftriaxone, 512 mg/ml ampicillin, 16 mg/ml nitrofurantoin, or 64 mg/ml cefazolin [97].

For cell lysis experiments, bacteria were spun down from the incubation chamber into the cell lysis chamber following sample entry.

2.2 Result and discussion

2.2.1 Valving

The laser valve mechanism is shown in Figure 2.3. Since the inner feature disc is fabricated from a black COC polymer, these valves are made by milling half of a channel on one side of the feature disc, and the subsequent half on the other side. These two half channels have an overlapping area separated by a 0.25 mm thick piece of COC. To open a valve, a laser is focused on the overlapping area called valve position, melting the thin COC piece. The energy required for opening each valve is nearly 1 Joule, estimated using equation 2.1.

$$Q_{tot} = Q_T + Q_F + Q_V = mc_p\Delta T + mL_F + mL_V \quad \text{(Eq 2.1)}$$

where cp is the specific heat of our material, ΔT is the change in temperature needed to melt the material, m is the mass of the valve, LF is the latent heat of fusion for our material, and LV is the latent heat of vaporization for our material. With our 1 W laser, and estimated efficiency of 20%, we require 5 seconds to open each valve. Positioning of the laser is accomplished by the coordinated movement of the linear actuator and the main motor, which step the radial position and angular position respectively. After melting away the valve material, the free flow of liquid is resumed.

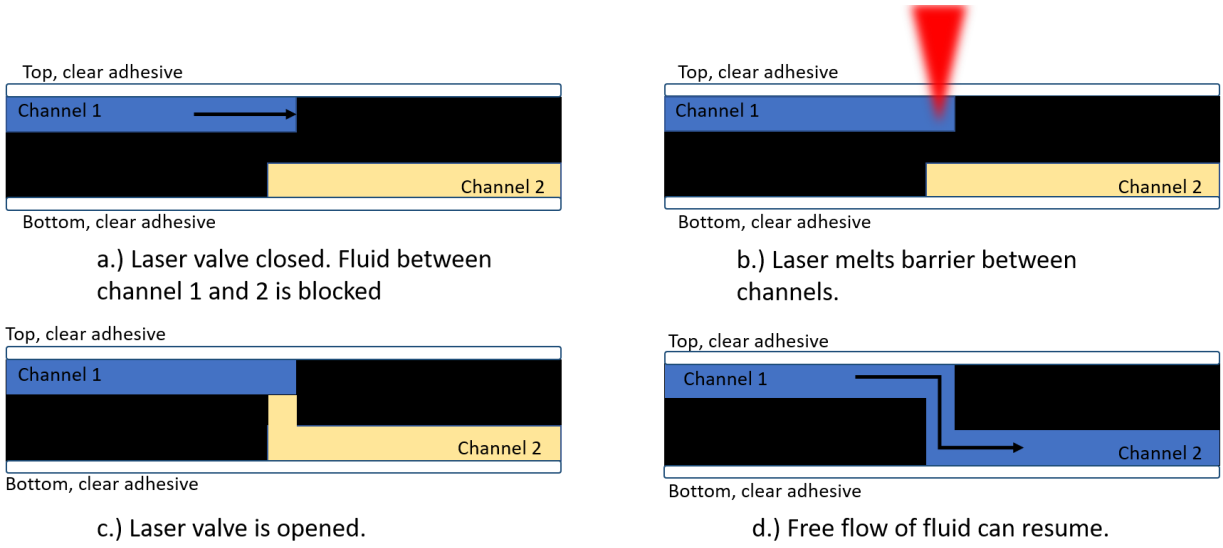

Figure 2.3. Working principle of the laser valve. a) Two half channels were machined on the different side of the black COC with an overlapping area covered by 0.25 mm thick plastic. b)- d) A laser melts the barrier between the channel and the valve is opened to resume the free flow of liquid.

2.2.2 Universal Cell Lysis

The bacteria cell wall has evolved to become one of the most resilient barriers against harsh environmental conditions filled with toxic contaminants. In fact, the origin of antibiotic resistance stems from this evolutionary response. For example, gram-negative bacteria are naturally more resilient to antibiotics than gram-positive bacteria due to their dual-layered cell envelope. The additional outer layer, absent in gram-positives, consists of an asymmetric lipid membrane formed by exterior-facing lipopolysaccharides and interior-facing phospholipids.

Due to the thicker cell wall of gram-positive bacteria, a combination of mechanical and alkaline chemical lysis is needed to release rRNA from cells. The mechanical component of our lysis system helps puncture and tear open the tough outer cell membrane of gram-positive bacteria by causing shear and friction forces between the cell wall and 100 μm

sized silica/zirconia beads (Figure 2.4b). Once the cell wall is obliterated, NaOH denatures the ribosomal complex, allowing the 16s rRNA fragment to be recovered (Figure 2.4c). Finally, the sample is neutralized with PBS to prevent rRNA hydrolysis by prolonged NaOH exposure (Figure 2.4d).

To optimize the lysis protocol for bacteria, we varied several parameters, including lysis time, spin speed of the disc (which determined the oscillation of the metal disc in the lysis chamber), silica/zirconia bead slurry amount (which determined the amount of grinding material for mechanical lysis), and lysis puck geometry. The results are shown for gram-positive isolate Staphylococcus aureus (SA15-21-08) in Figure 2.5 and expressed as a percentage of the Luminex signal obtained using the Omnilyse commercial lysis system (Claremont BioSolutions, LLC, CA, USA). As a control, chemical lysis (1 M NaOH) is shown as well. The results of the optimization experiments were used to determine an optimal universal lysis system, with characteristics summarized in Table 2.1.

Finally, to demonstrate our universal lysis system, we lysed several gram-positive bacteria, including 2 strains of Staphylococcus aureus (SA), a strain of Coagulase-negative staphylococcus (CNS), a strain of *Streptococcus agalactiae* (Sagal), and a strain of *Enterococcus* (EFs), see Figure 2.6. While lysis efficiency on the disc varied, all strains showed lysis efficiency at least 75% of the Omnilyse system.

Table 2.1 Optimized parameter for lysis

Parameters	Value
Lysis time	6 min
Spin speed	100 RPM
Bead amount	120 µl
Metal disc geometry	Double

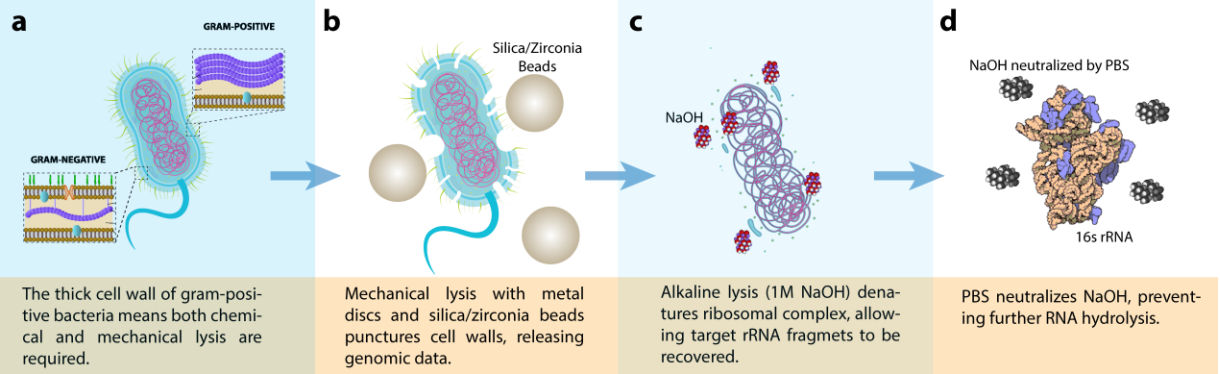

Figure 2.4. Universal lysis schematic. a) The thick cell wall of gram-positive bacteria means both chemical and mechanical lysis are required, b) Mechanical lysis with metal discs and silica/zirconia beads punctures cell walls, releasing genomic data, c) Alkaline lysis (1M NaOH) denatures ribosomal complex, allowing target rRNA fragments to be recovered, d) PBS neutralizes NaOH, preventing further RNA hydrolysis.

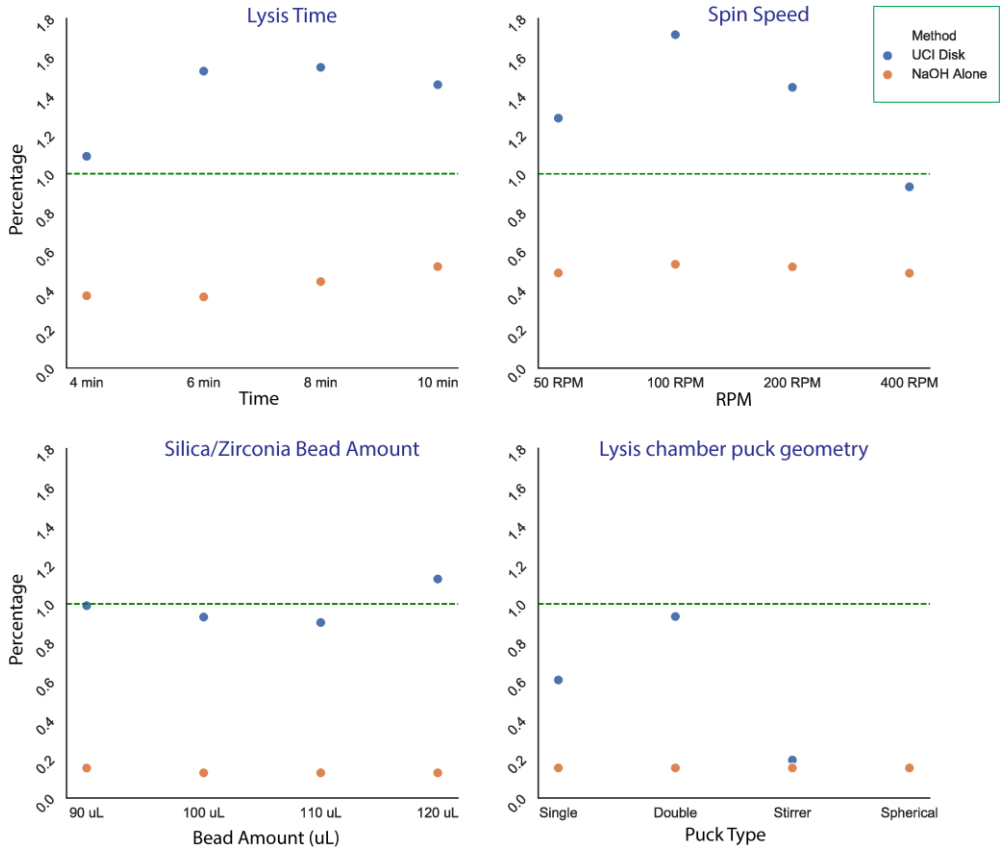

Figure 2.5. Optimizing lysis efficiency. Both chemical lysis and chemical mechanical lysis of *E. Coli* were tested against the Omnilyse cartridge for a series of parameters. All measurements are shown as a percentage of the omnilyse cartridge signal, which has been normalized to 100% (dotted green line). a) Total lysis time was varied from 4-10 minutes. b) Total spin RPM was varied from 50-400

RPM. c) Total Silica/Zirconia bead slurry was varied from 90-120 µL pipetted into the lysis chamber. d) Several puck geometries were tested, including a single or double thin steel disc, a magnetic stir bar, or a spherical steel disc.

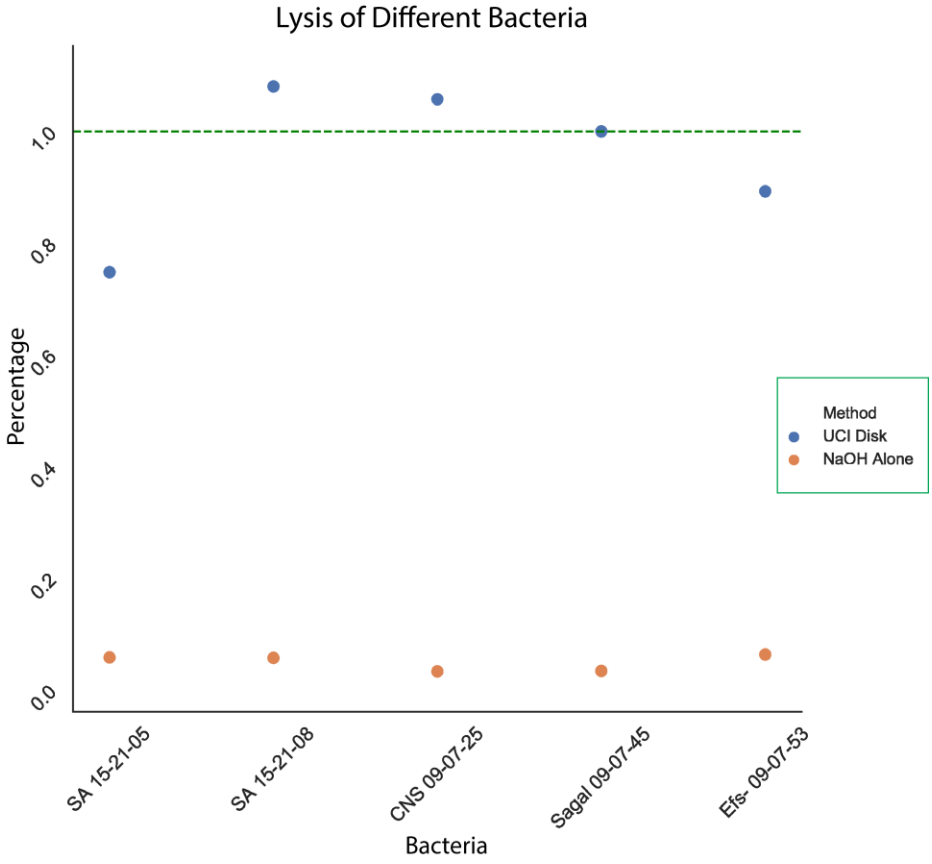

Figure 2.6. 6 gram-positive isolates were compared with chemical lysis alone and chemical mechanical lysis, including 2 Staph. aureus (SA), 1 Coagulase-negative staphylococcus (CNS), 1 *Strep. agalactiae* (Sagal), and 1 *Enterococcus* (EFs). All measurements are shown as a percentage of the omnilyse cartridge signal, which has been normalized to 100% (dotted green line).

2.2.3 Rapid Bacteria Incubation

For liquid bacterial cultures, rapid and healthy growth depends on three main parameters: 1.) Sample aeration: A bacteria sample needs to have plenty of access to fresh oxygen for growth, 2.) Nutrient availability: A sample needs to be thoroughly mixed in order to provide nutrients equally to all parts of the culture, and 3.) Prevention of biofilms and

clumping: Shaking and agitation can prevent bacteria culture from settling to the bottom of a chamber and forming biofilms or clumps that hinder reproduction.

The low Reynold numbers in microfluidic systems exhibit laminar flow regimes, which are dominated by viscous forces, rather than inertial forces. The absence of turbulence makes healthy and rapid bacterial growth particularly challenging and forces microfluidic devices to rely on either passive molecular diffusion or external energy sources for mixing [98,99]. Furthermore, the small, enclosed volumes characteristic of microfluidic systems restricts access to fresh oxygen, making sample aeration difficult without bulky or complex external pumps that bubble oxygen through a sample [100].

To optimize incubation, while keeping within the available real estate of the portable disc, the incubation chamber characteristics in Table 2.2 were chosen. The angular span was maximized while still keeping 6 multiplexed sections on the disc, and r1 and r2 were restricted by the need for fitting all assay steps onto the chosen disc radius of 60 mm. The incubation chamber was also milled completely through the inner feature disc, allowing for a large surface area of the chamber to be covered by a gas-permeable membrane.

Table 2.2 Optimized parameter for incubation

Parameters	Value
Inner radius (r_1)	6 min
Outer radius (r_2)	100 RPM
Acceleration/deceleration rate	240 rad/s
Angular span (θ_I)	45°

We compared the growth using our chosen CD chamber design and oscillation protocol to cultures grown in a 96-well plate and CD placed into a standard incubator at 400 RPM. Observation of fluid within the different configurations showed more turbulence and

advection in the disc in the SpinBox than in either the 96-well plate or disc in the SpinBox. Figure 2.7 shows a significant increase in rRNA growth of the disc on the spinstand at both 60 and 90 minutes compared with the other configurations. At 90 minutes, an average 162% increase in rRNA was observed in the incubator spinstand compared with a 96-well plate on the plate shaker incubator. The incubator disc in the SpinBox showed an average 122% increase in rRNA after 90 minutes compared to the 96-well plate, demonstrating that both the type of mixing and aeration have an effect on bacterial growth.

To ascertain that the effect was not isolated to a single *E. Coli* strain, we compared growth on the disc and the 96-well plate in 14 different strains of *E. coli*, see Figure 2.8. The graph compares cfu/mL on the disc (y-axis) vs. the 96-well plate (x-axis). The red dotted line has a slope of 1 (y = x) and represents bacteria growing equally on the plate and on the disc. All data points above the red dotted line represent strains that grew better on the disc and data points below the red dotted line represent strains that grew better on the 96-well plate. The majority of the isolates tested showed more than 2x better growth on the disc than the 96-well plate. Two strains of *E. Coli* showed worse growth on the disc than on the 96-well plate. This might be either an outlier or might represent bacterial strains that favor alternative growth conditions. However, despite the growth characteristics of these *E. coli* strains, the measured cfu/mL, compared with the 0-minute time point, is sufficient to test antibiotic susceptibility.

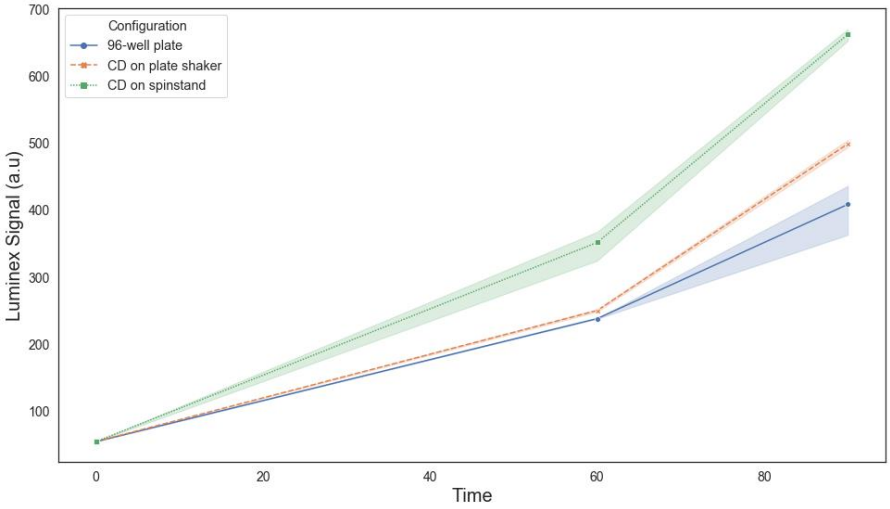

Figure 2.7. Comparing *E. Coli* growth on the 96-well plate in the plate shaker incubator, the disc in the plate shaker incubator, and the disc on the incubator spinstand. Growth is shown as Luminex signal intensity. Shading represents error bars.

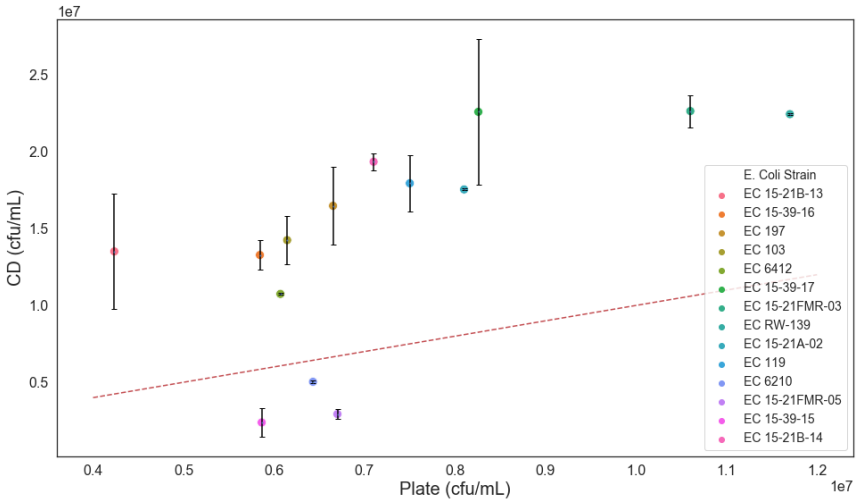

Figure 2.8. Growth for 14 different strains of *E. coli* in the disc on the incubator spinstand is compared with growth on the 96-well plate in the plate shaker incubator. The dotted red line (y = x) has a slope of 1, with data points above it showing greater growth on the disc, and data points below it showing greater growth on the plate. Growth is shown in colony-forming units per milliliter (cfu/mL).

Chapter 3

Recirculation mechanism for fluidic manipulation and hybridization enhancement

3.1 Background of hybridization process on microarrays

Microarray technologies have been widely investigated as a powerful tool to simultaneously detect the presence of multiple different molecules such as nucleic acids (DNA, RNA) and proteins (antibodies) [101]. With the capture probes spotted on specific locations, the microarrays are spatially encoded to enable multiplexing. In most cases, species-specific capture probes are spotted on the substrates which are usually made of glass, plastic, silicon, or nitrocellulose membrane [102,103]. These two-dimensional substrates allow decoding with optical detection methods, however, have low efficiency in hybridization. After the initial reaction-limited period, the low diffusion coefficients of molecules, which have an order of $10^{-7}cm^2s^{-1}$ for proteins and DNAs, lead to a diffusion-limited process by forming a depletion layer over the substrate [104,105].

Microfluidics technologies apply a confined space above the microarrays to reduce the diffusion distance. Beyond that, the depleted layer is replenished with molecules as the molecule-abundant solution moves over the surface[101,106]. In centrifugal microfluidics, this fluid movement was achieved by switching liquid in the loading chamber and compression chamber and creating a reciprocating flow of liquid over the microarray [73]. It was further developed by Aeinehvand et al. that replaces the large compression chamber

with a latex balloon, which saves on-disc real estate, enables larger reaction volume, enhances mixing, and reduces the workload of motor [65]. However, such methods characterize a dead volume in the loading chamber and channel, as they must maintain the difference in liquid column height to balance the pressure in the compression chamber. Another limitation lies in the flow, which characterizes a low Reynolds number, indicating a laminar flow and the formation of a boundary layer that inhibits thorough mixing. Moreover, the porous nitrocellulose membranes which are used in protein microarrays to increase capture probe loading, trap liquid like a sponge, further discourage the mixing of the solution.

An alternative approach is called recirculation, by removing the depletion layer through draining the probe solution and replenishing it with a probe-abundant solution to resume quick binding [107]. In this chapter, we introduced an inward pumping mechanism that uses an elastic membrane to recirculate liquid. This mechanism also features a high inward pumping efficiency of 78-89% and a mixing capability. A design that combines the inward pumping and blood/plasma separation was also evaluated as a potential application for the described fluid rerouting mechanism. Preliminary tests were conducted to show the potential fluidic enhancement to the hybridization process from the recirculation motion of the liquid.

3.2 Working principle

Schematic drawings of the recirculation mechanism for inward pumping enabled by an elastic membrane cover and the relevant sequence of fluidic steps are shown in Figure 3.1. The CD design in Figure 3.1a consists of seven components: inlet hole, loading chamber,

inlet channel with high fluidic resistance, recirculating chamber with elastic membrane cover, recirculating channel with low fluidic resistance, ventilation hole, and collection chamber. The working principle of the mechanism is shown in Figure 3.1b. Step 1: the liquid is introduced to the loading chamber through the inlet hole. Step 2: the CD spins at high rpm to propel the liquid into the recirculating chamber and inflate the elastic membrane. Step 3: upon fast deceleration, the return of the elastic membrane to its initial position pushes the liquid from the recirculating chamber towards the center of the CD through the two channels that have distinct resistances – a wider channel has lower fluidic resistance than the narrower winding channel of higher fluidic resistance. As the volumetric flow rate of liquid is much higher in the channel with lower resistance (recirculating channel), most of the liquid is pumped inwards through the recirculating channel and arrives at the collection chamber, as seen in Step 4. The liquid left in the loading chamber and recirculating chamber can be further pumped inwards by repeating cycles from Step 2 to Step 4, denoted as the recirculating cycles.

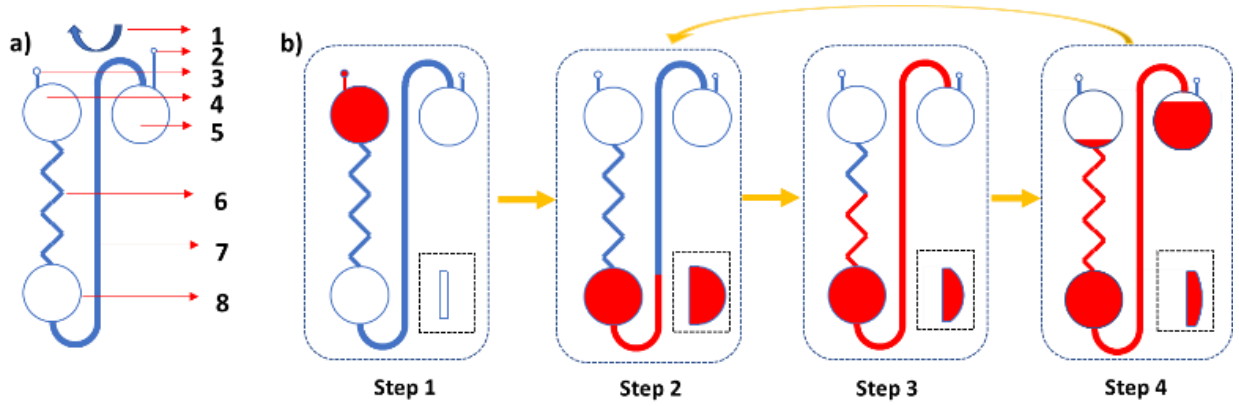

Figure 3.1. Schematic drawing of the recirculation mechanism for inward pumping. a) The layout of the inward pumping design: 1. The center of rotation. 2. Ventilation hole. 3. Inlet hole. 4. Loading chamber. 5. Collection chamber. 6. Inlet channel with high fluidic resistance. 7. Recirculating channel with low fluidic resistance. 8. Recirculating chamber with an elastic membrane cover. b)

The working principle of inward pumping. The dashed boxes show the side view of the recirculating chamber at each step (not to scale). Step 1: Sample liquid is injected into the loading chamber through an injection hole. Step 2: The CD is spun at high speed. The liquid in the loading chamber flows through the inlet channel to fill the recirculating chamber and inflate the elastic membrane. Step 3: The angular velocity of the CD decreases rapidly to release the energy that was stored in the membrane. As the elastic membrane returns to its original position, the liquid is pumped inwards through both the inlet and recirculating channels. Step 4: Since fluid in recirculating channel flows faster than in the inlet channel, most of the liquid is pumped inwards through this channel to the collection chamber. After step 4, recirculating cycles step 2-4 can be conducted to achieve higher inward pumping efficiency.

To evaluate the hybridization efficiency of different fluidic profiles, we conducted a preliminary test by comparing the reciprocation and the recirculation flow of the liquid. The recirculation mechanism was modified to remove liquid from the reaction area and replenish it from the top. As shown in Figure 3.2a, the liquid was redirected by the recirculation channel to the loading chamber and it is ready for spin down again. A microarray integrated design is shown in Figure 3.2b, allowing the complete removal of liquid over the microarray chamber and replenishing from the loading chamber at next cycle.

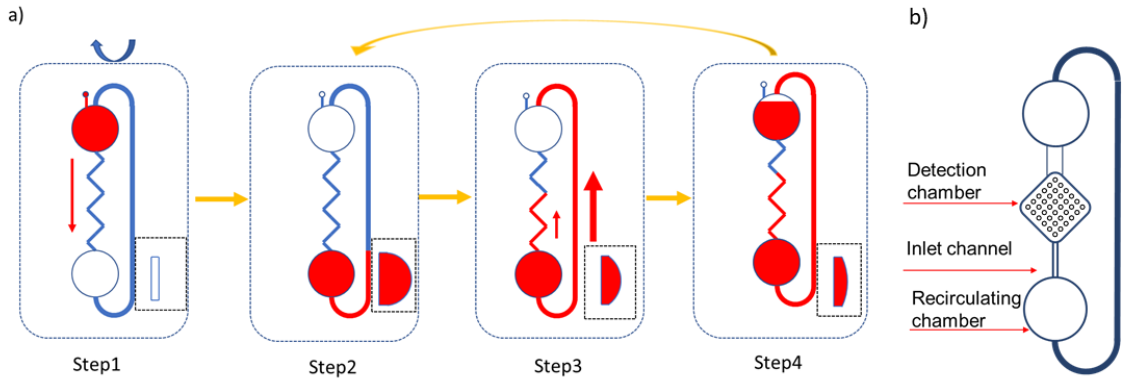

Figure 3.2. Schematic drawing of the recirculation mechanism for hybridization on a microarray. a) By guiding the recirculating channel into the original chamber, liquid can be reloaded into the loading chamber for the next cycle. b) a schematic design for testing hybridization efficiency. A microarray chamber is sitting between the loading chamber and recirculating chamber, which allows the complete removal of probe solution and replenishing from the loading chamber at the next cycle.

3.3 Materials and methods

3.3.1 CD design and fabrication

To investigate the elastic membrane-enabled recirculation mechanism, various CD designs were fabricated and tested. CDs with a radius of 40 mm were designed in SolidWorks (Dassault Systèmes SOLIDWORKS Corp.) and assembled as shown in Figure 3.3. The top and bottom CD were machined from PMMA sheets (McMaster-Carr, CA, USA) with a CNC mill (PCNC 440, Tormach Inc., WI, USA) utilizing the G-code generated by SolidCAM (SolidCAM Ltd., USA). For elastic membrane covers, silicone rubber (McMaster-Carr, CA, USA) and natural rubber (McMaster-Carr, CA, USA) were cut into circles with the desired radius. Double-sided pressure-sensitive adhesives (FLEXmount® DFM 200 Clear V-95 150 Poly H-9 V-95 400 Poly H-95 4, FLEXcon, MA, USA) were cut into desired circular shapes for the ring adhesive layer and intermediate bonding adhesive layer with a cutter plotter (Silhouette Cameo 4, Silhouette America, Inc., UT, USA). The cutter plotter was also used to cut the bottom adhesive layer with single-sided pressure-sensitive adhesive (3MTM 9795R, 3M, MN, USA). After machining, the CDs were cleaned with DI water and isopropyl alcohol (Sigma Aldrich, MO, USA). The ring adhesives were placed on the shallow terrace at the top CD to bond with the elastic membrane cover. The intermediate bonding adhesive layer was then applied between the top and bottom CD, with the features on both CDs and adhesive being carefully aligned. The bottom adhesive layer was applied on the bottom CD, covering the channels and chambers. The assembled CD was then subjected to pressing five times with a roller press (Dayton's DC Speed Control Roller, Dayton Electric Mfg Co., IL, USA) to

ensure strong bonding. After the pressing, the CD was placed under ambient temperature for 24 hours before testing.

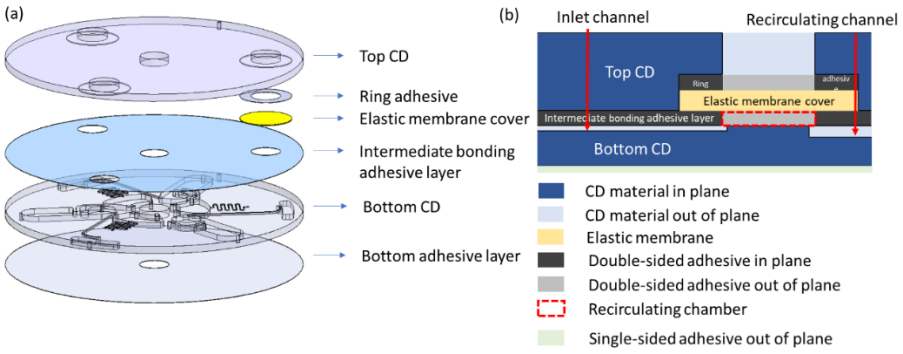

Figure 3.3. Layout for CD assembly. (a) Detailed layout of the CD components. (b) A schematic cross-sectional view of the recirculation chamber. The red dashed square indicates the recirculation chamber, which has a thickness of 100 μm.

3.3.2 CD testing platform

A centrifugal microfluidic spinstand that we previously reported was used to conduct and observe the experiments (see Appendix B) 28. A brushless DC motor (Anaheim Automation Inc., CA, USA) was controlled by a brushless DC controller (EZSV23, AllMotion, CA, USA) to spin the CDs. To observe the microfluidic flow on the CDs, a piece of 5 mm wide reflective aluminum adhesive tape (Sigma Aldrich, MO, USA) was placed at the edge of the CD. An IR sensor (PBT46U, Banner Engineering Corp., MN, USA) sending and receiving an IR beam was placed beneath the edge of the CD as the trigger for the camera's shutter, thus triggering one snapshot of the disc per revolution. A camera (aca800-510uc, Basler, Inc., PA, USA) and a stroboscope (DT-311A, Shimpo Instrument, NY, USA) were used to take pictures when they received the signal from the sensor. Image processing software ImageJ was used to analyze the images.

3.3.3 Inward pumping efficiency test

The schematic drawing of the so-called "quantification design" (qCD) is shown in Figure 3.4a. This design is intended to pump liquid inwards from a radial distance of 34 mm to a radial distance of 14 mm from the center. The pumping efficiency η is calculated as:

$$\eta = \frac{V_{transferred}}{V_{initial}} \quad \text{(Eq 3.1)}$$

where $V_{initial}$ is the volume of fluid initially placed in the loading chamber, and $V_{transferred}$ is the volume of fluid that is pumped into the collection chamber with the leftover volume calculated as:

$$V_{leftover} = V_{initial} - V_{transferred} \quad \text{(Eq 3.2)}$$

The collection chamber was designed with a uniform depth so that the transferred volume can be calculated by measuring the area that the liquid covers through processing the images of the chambers taken at the beginning and the end of the fluid transfer process. To minimize the leftover volume in the recirculating chamber, this chamber was designed to reach a minimum volume when the elastic membrane cover pushes against the bottom CD surface when the CD is stationary. The height of the recirculating chamber corresponds to the thickness of the bonding adhesive, which is 100 μm. After loading the qCD with DI water of various volumes where dye (McMaster-Carr, IL, USA) was added for ease of observation, the tests were conducted with a protocol consisting of alternating the spin speed between 3600 rpm and 180 rpm, as shown in Figure 3.4e and Appendix B table B1. Once this protocol was finished, the qCD was spun at 1000 rpm again to form a uniform

meniscus in the collection chamber. Images of the quantification chambers were taken at this spin speed to calculate the volume of transferred liquid.

3.3.4 Recirculation/mixing efficiency test

The recirculation and mixing tests were conducted with a CD design (rmCD) presented in Figure 3.4b. The recirculating channel was designed to guide the liquid back to the loading chamber to complete the recirculation of liquid. To visualize the mixing effect better, a light-colored natural rubber membrane (McMaster-Carr, IL, USA) was used as the elastic membrane cover for the recirculating chamber. 50 µl of DI water with green dye (McMaster-Carr, IL, USA) was first injected in the loading chamber through the inlet hole. The CD was spun at 2000 rpm to propel the liquid down to the recirculating chamber. The rmCD was then slowly stopped so that the liquid did not travel through the recirculating channel. 50 µl of DI water with blue dye (McMaster-Carr, IL, USA) was slowly loaded in the loading chamber through the inlet hole without disturbing the previously loaded liquid. The rmCD was then tested on the spinstand with the same protocol as the inward pumping efficiency test (the spin profile is presented in Figure 3.4e).

3.3.5 Blood/plasma separation and transfer test

The CD design of blood/plasma separation CD (bpsCD) is shown in Figure 3.4c. While similar in design to the qCD, the bpsCD has a blood cell chamber with a volume of 75 µl that connects to the bottom of the recirculating chamber. 150 µl of bovine blood (Sigma Aldrich, MO, USA) was injected into the loading chamber through the inlet hole. Blood/plasma separation and transfer tests were conducted using the spin protocol shown in Figure 3.4f,

where during the plasma separation step, the bpsCD is spun at 4500 rpm for 5 minutes. After the test, the bpsCD was spun at 1000 rpm to take quantification images.

3.3.6 Hybridization tests for various fluidic profiles

The hybridization tests were conducted with the designs shown in Figure 3.5. To investigate the hybridization process with recirculation mechanism, a CD with a ventless chamber (Figure 3.5c) was designed based on the inward pumping mechanism reported by Zehnle et al. [63]. For different CD designs, tests were conducted with different protocols shown in Appendix B Table B3. We adopted an ELISA that targets Sars-CoV-2 IgG antibodies with the hybridization process shown in Appendix B Table B4. The microarray was spotted with SARS-CoV2. RBM.mFc antigens and the layout is shown in Appendix B Figure B2.

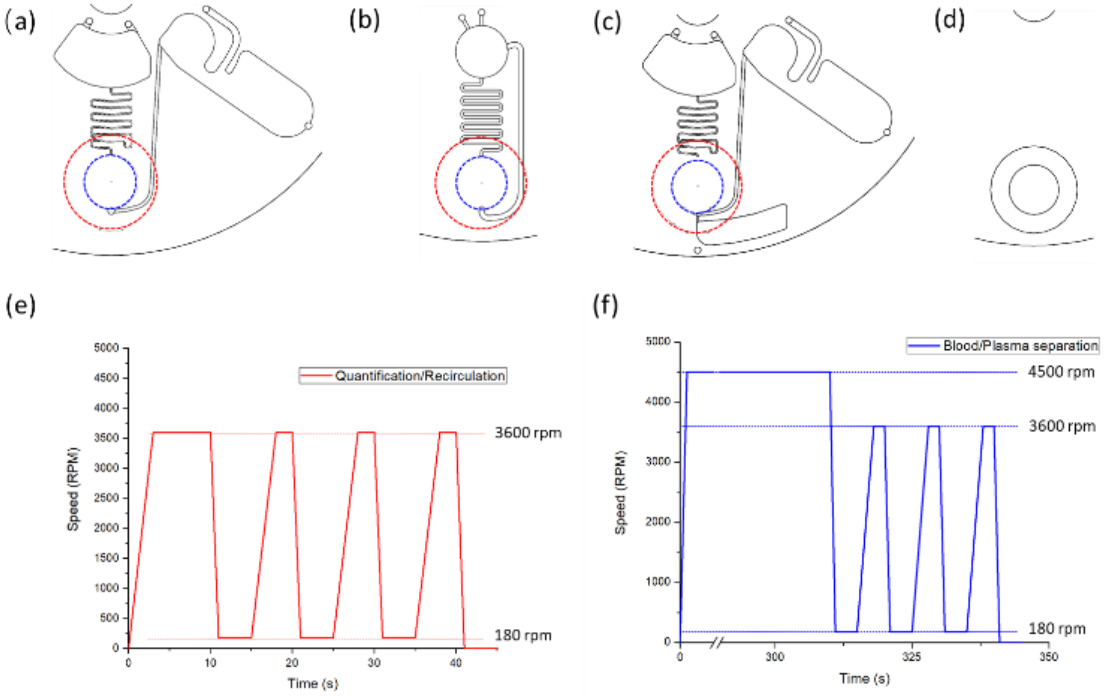

Figure 3.4. a), b), c) various CD designs. The blue dashed circles indicate the position of the recirculation chamber, and red dashed circles indicate the position of the terrace on the top CD. a) CD design of quantification CD (qCD). The recirculating channel guides the liquid to a collection chamber. b) CD design for recirculation/mixing CD (rmCD). The recirculating channel guides the liquid back to the loading chamber. c) CD design for blood/plasma separation CD (bpsCD). A chamber connecting to the bottom chamber with a small channel was designed to collect the blood cells. d) Design of the top plastic layer for all CD designs that contain a terrace to place the ring adhesive and elastic membrane. A trough hole leaves enough space for the inflation of the elastic membrane cover. e) Protocol for quantification test and recirculation/mixing test. The detailed protocol is provided in Appendix B Table B1. f) Protocol for blood/plasma separation test. The CD is spun at 4500 rpm to perform blood/plasma separation. The detailed protocol is provided in Appendix B Table B2.

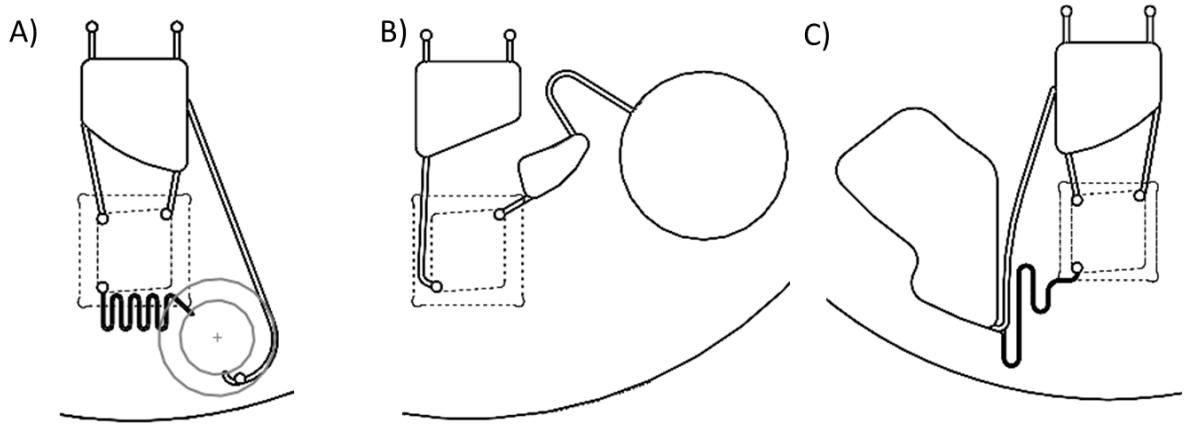

Figure 3.5. Designs for hybridization test. Three designs: a) Recirculation with elastic membrane, b) reciprocation with ventless chamber, and c) recirculation with ventless chamber are machined and fabricated. Two different protocols were used to conduct the hybridization cycles, which is listed in Appendix B Table B3

3.4 Results and discussion

3.4.1 Inward pumping efficiency

Experiments were conducted to evaluate the inward pumping efficiencies with various initial volumes. To calibrate the camera and image processing software, 80µl, 100µl, 120µl, 140µl and 160µl of the colored DI water were separately loaded into the quantification chamber directly from the ventilation hole. Images were taken with the qCD spinning at 1000 rpm to generate a calibration line (as shown in Appendix B Figure B3). The inward

pumping efficiency tests were conducted with various initial volumes: 100µl, 120µl, 140µl, and 160µl. The plots of the corresponding transferred volumes of the fluid, the inward pumping efficiency values, and the leftover volumes are presented in Figure 3.6.

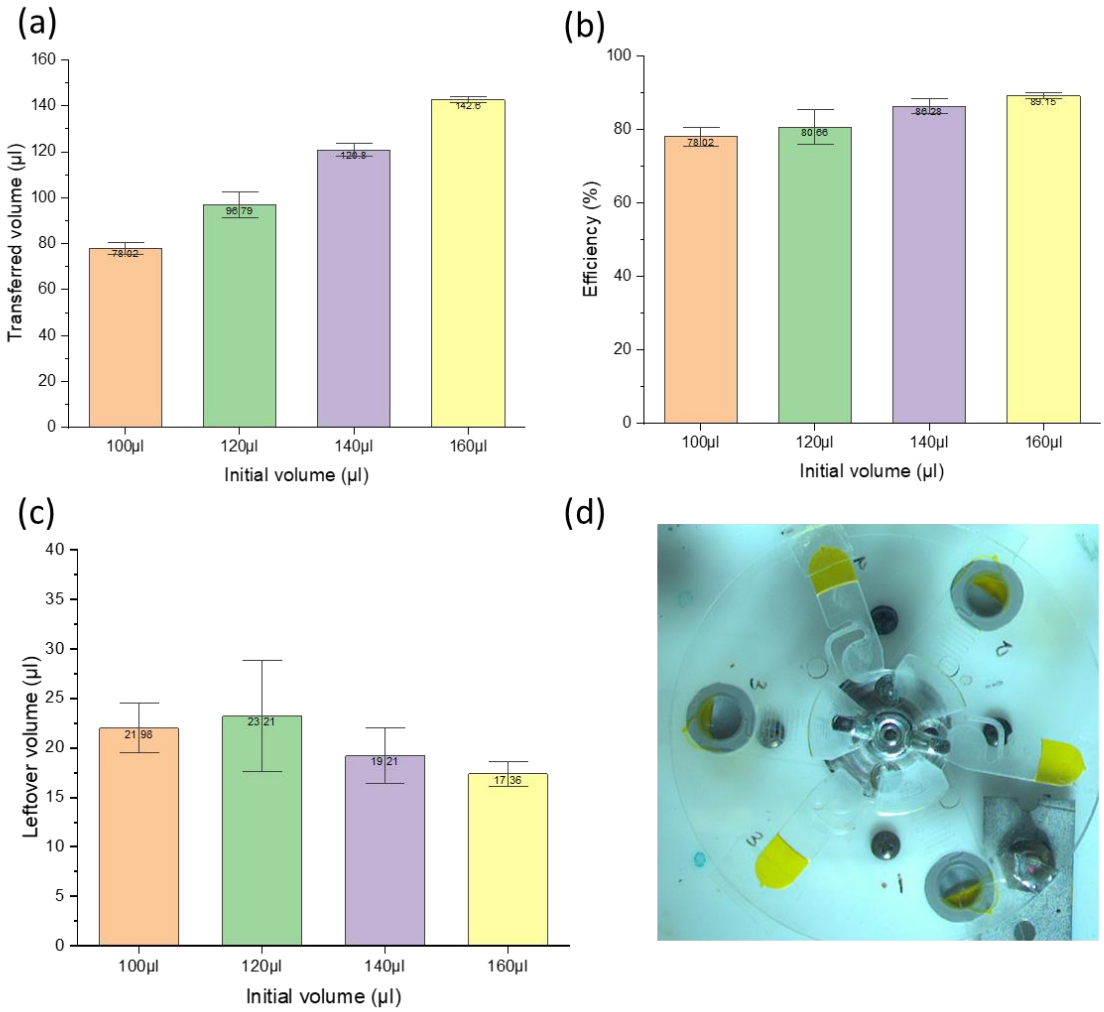

Figure 3.6. The inward pumping efficiency tests were conducted with colored DI water. Transferred volumes a), inward pumping efficiencies b), and leftover volumes c) are presented on the respective plots. As the initial volume gets larger, the transfer efficiency gets higher. On the other hand, the leftover volume does not change much as the initial volume varies. A representative image d) demonstrates the liquid transfer at 1000 rpm. The error bars shown in the graph represent one standard deviation.

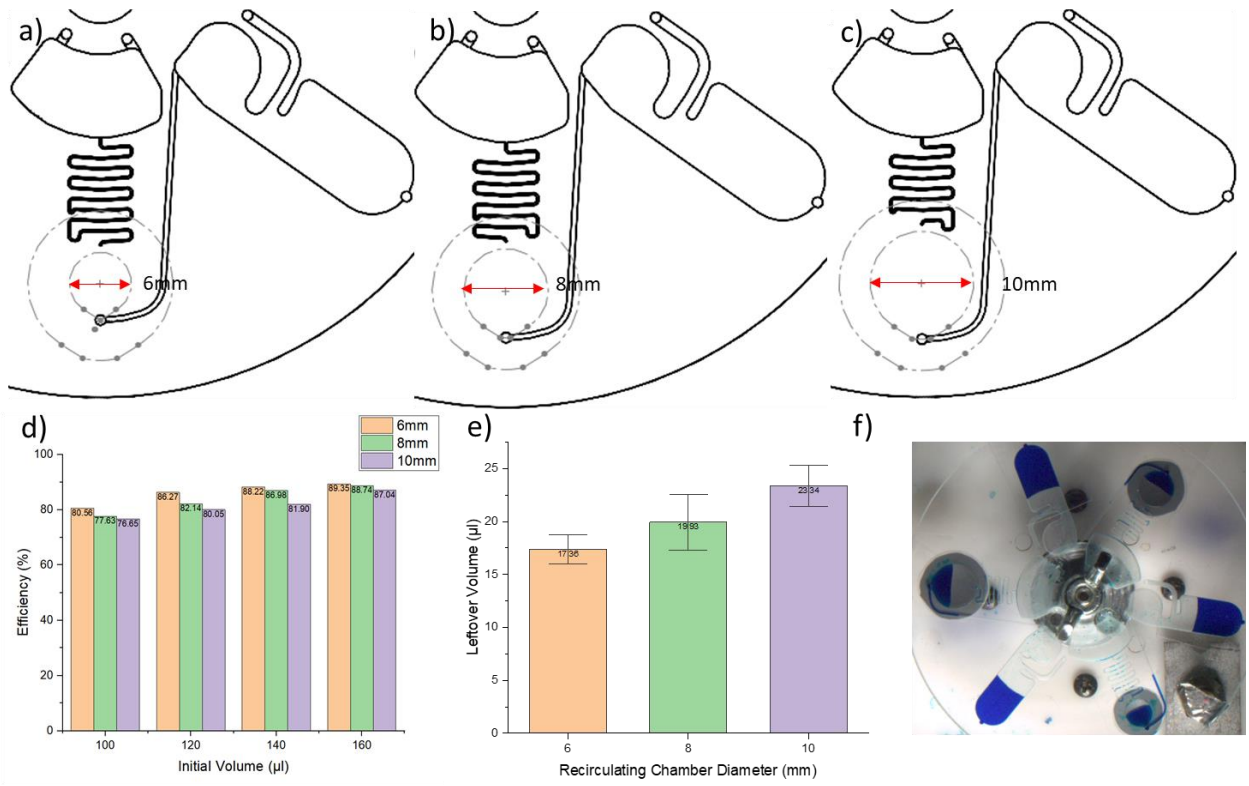

Figure 3.7. Inward pumping efficiency designs for CD designs with different diameters of recirculating chambers: a) 6 mm, b) 8 mm, and c) 10 mm. The inward pumping efficiency and the leftover volume for each design are shown in d) and e). As the recirculating chamber becomes bigger, the inward pumping efficiency decreases, and the leftover volume increases. A representative screenshot of the tests is shown in f). The error bars in e) correspond to one standard deviation.

As shown in Figure 3.6b, with the current design and protocol, the inward pumping efficiency increased from 78% to 89% as the initial volume increased from 100µl to 160µl. Meanwhile, the leftover volume shown in Figure 3.6c remained approximately the same. To further investigate the influence of the size of the elastic membrane on pumping efficiency, recirculating chambers with different sizes were designed (see Figure 3.7a-c). The inward pumping efficiencies and leftover volumes for each design are presented in Figure 3.7d and 3.7e. An overall trend can be observed that, as the initial volume increases, the inward pumping efficiency increases, which agrees with the result shown in Figure 3.6b. Another trend revealed by these experiments is that the leftover volume grows with the size of the

recirculating chamber. At the same time, the leftover volume remained approximately the same for the same chamber size, despite different initial volumes.

To analyze the process of elastic membrane enabled inward pumping, screenshots at crucial time points during an inward pumping efficiency test with 140 µl as initial volume are presented in Figure 8. Firstly, the liquid is loaded into the loading chamber, as shown in Figure 3.8a. Then the qCD is spun at 3600 rpm, and the liquid transfers to the recirculating chamber, as shown in Figure 3.8b. After fast deceleration to 180 rpm, the liquid travels inwards through both the inlet and recirculating channels, as shown in Figure 3.8c. The liquid filled the entire recirculating chamber and not only entered the collection chamber through the recirculation channel but also entered the loading chamber through the inlet channel (indicated by a red circle in Figure 3.8c). Then the qCD was spun at 3600 rpm again to push the fluid into the recirculating chamber, stretching the elastic membrane cover. Since the volume left to be transferred was smaller than the initial volume, the liquid level in the recirculating chamber in Figure 3.8d was lower than the liquid level in Figure 3.8b. The smaller liquid volume further led to an insufficient liquid filling of the entire recirculating chamber, thus decreasing the amount of stretch of the elastic membrane. Observation found that no liquid was able to flow to the loading chamber at 180 rpm, as shown in Figure 3.8e. In the meantime, there are some remaining liquid drops in the inlet channel that were not transferred to either the loading chamber or the recirculating chamber during the deceleration step. When a steady state was reached, a small meniscus appeared at the entrance of the collection chamber (inside the red circle in Figure 3.8e), providing surface tension to balance against the compression from the elastic membrane and the centrifugal force from the spinning of the CD. It indicates that the deformation of

the elastic membrane in Figure 3.8d is significant enough to push liquid into the collection chamber. At the end of the third 3600 rpm-180 rpm cycle, the meniscus shown in the red circle from Figure 3.8g is smaller than the meniscus in Figure 3.8e, indicating that the energy stored from the previous step shown in Figure 3.8f was not enough to pump any liquid further into the collection chamber. Thus, the inward pumping of liquid was completed.

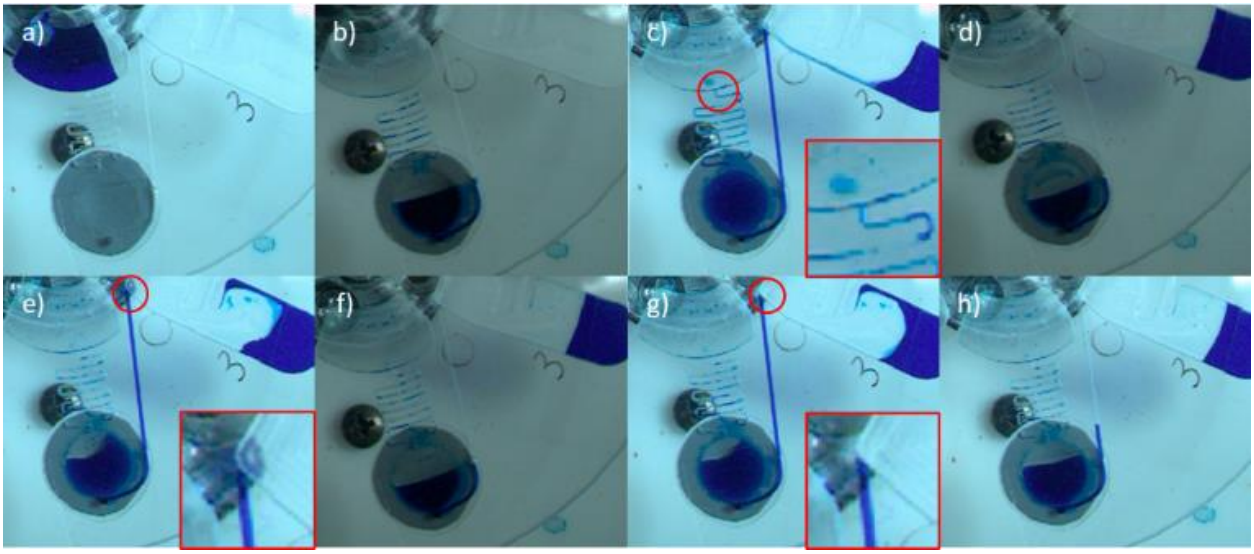

Figure 3.8. Screenshots of inward pumping efficiency test with 140µl of colored DI water. a) Loading of liquid into the loading chamber. b) During the high-speed step at 3600 rpm, the liquid was transferred from the loading chamber into the recirculating chamber. c) When the angular velocity was slowed to 180 rpm, liquid entered the loading chamber through the inlet channel as indicated by the red circle. The insert presents the magnified view of the circled region of the image. d) During the second high-speed step at 3600 rpm, less liquid was stored in the recirculating chamber to inflate the elastic membrane. e) When the disc's rotation was slowed to 180 rpm again, there was not enough of the liquid to fill the recirculating chamber. A meniscus appeared at the boundary of the recirculating channel and collection chamber, indicating the energy was still enough to pump liquid inwards. The insert presents the magnified details of the meniscus leading into the collection chamber. f) During the third high-speed step at 3600 rpm, followed by g) the third low-speed step at 180 rpm, no more liquid could be transferred into the collection chamber. The insert presented a magnified view of the recirculation channel joining the collection chamber, indicating no further fluid transfer is taking place. h) After the completion of the fluid transfer tests, the qCD was spun at 1000rpm to take quantification images.

Generally, the starting condition of a recirculating cycle can be categorized into two cases, depending on the volume of liquid left to be transferred. The first case is that with an initial liquid, V_{I1}, the elastic membrane stores enough energy during step 2, which can push the liquid to fill the recirculating chamber and flow back through the inlet channel when the CD decelerates during the Step 3 and 4. But, as the resistance of the inlet channel is significantly larger than the resistance of the recirculating channel, most of the liquid will be transferred through the recirculating channel, as denoted with V_{T1}. The volume left to be transferred, which is $V_{I1} - V_{T1}$, will be the initial volume V_{I2} of the next cycle. As the cycles continue, the liquid leftover volume gets smaller. Eventually, the initial volume of a cycle will not be enough to fill the entire recirculating chamber during the deceleration step, which can be categorized as the second case. In this case, the deformation of the elastic membrane is not large enough to push liquid columns in trenches and bends of the inlet channel to move inwards. These liquid columns, which are called liquid plug valves by other researchers, create a high hydraulic resistance that blocks the channel and prevents any backflow of liquid[108]. Therefore, the energy stored in the elastic membrane can only transfer liquid through the recirculating channel. A final equilibrium stage is reached when a balance is achieved among the pressure generated by the elastic membrane, the pressure head generated by the centrifugal forces on the disc, and the pressure caused by the capillary force.

We conducted a conservative analysis of the equilibrium at the slow-speed (180 rpm) step of the final cycle. To estimate the range of possible leftover volumes, we made several assumptions to simplify the calculation. Firstly, the inlet channel was considered blocked

by the liquid plug valves per the previous discussion. Then to estimate the largest leftover volume, the recirculating chamber was assumed to be filled with liquid at the equilibrium stage. Another assumption was that the shape of the elastic membrane is spherical, which is close to reality when the CD was spun at a low speed, such as 180 rpm. The liquid volume in the inlet channel was neglected in this calculation, as its total volume is 2.98μl and most of it is occupied by air. Therefore, the pressure generated by the deformation of the elastic membrane, P_m, in terms of the bulge height, h, can be calculated as follows[65,109,110]:

$$P_m(h) = C_1 \frac{Mth^3}{a^4} + C_2 \frac{\sigma_0 th}{a^2} \quad \text{(Eq 3.3)}$$

t is the thickness of the membrane. a is the radius of the recirculating chamber. C_1 and C_2 are geometrical constants. M is the biaxial modulus of the elasticity of the membrane, which can be calculated using Young's modulus of elasticity E and Poisson's ratio ν:

$$M = \frac{E}{1-\nu} \quad \text{(Eq 3.4)}$$

The pressure balance at equilibrium can be described as:

$$P_m = P_c + P_{cap} \quad \text{(Eq 3.5)}$$

P_c is the centrifugal pressure generated by the liquid column equal to (for the filled recirculating chamber):

$$P_c = \frac{1}{2}\rho\omega^2[((r_2 - a)^2 - r_1^2)] \quad \text{(Eq 3.6)}$$

while P_{cap} is the capillary pressure that can be described as follows[42,111]:

$$P_{cap} = -\frac{3\sigma cos\theta_p^* + \sigma cos\theta_a}{4l} \quad \text{(Eq 3.7)}$$

where ρ is the density of the liquid, ω is the angular speed of the CD, r_1 is the radial position of the exit of the recirculating channel, r_2 is the radial position of the center of the recirculating chamber, σ is the surface energy of the water/air interface, θ_p^* is the contact angle at the exit of the recirculating channel, described by $\theta_p^* = \min\{\theta_p + \beta, 180°\}$[42], θ_p is the contact angle of water/PMMA, β is the angle change at the exit of the recirculating channel, θ_a is the contact angle of water/adhesive[111], and l is the width and height of the recirculating channel with a square cross-sectional area. A schematic drawing relating to the outlined analysis is presented in Figure 3.9a.

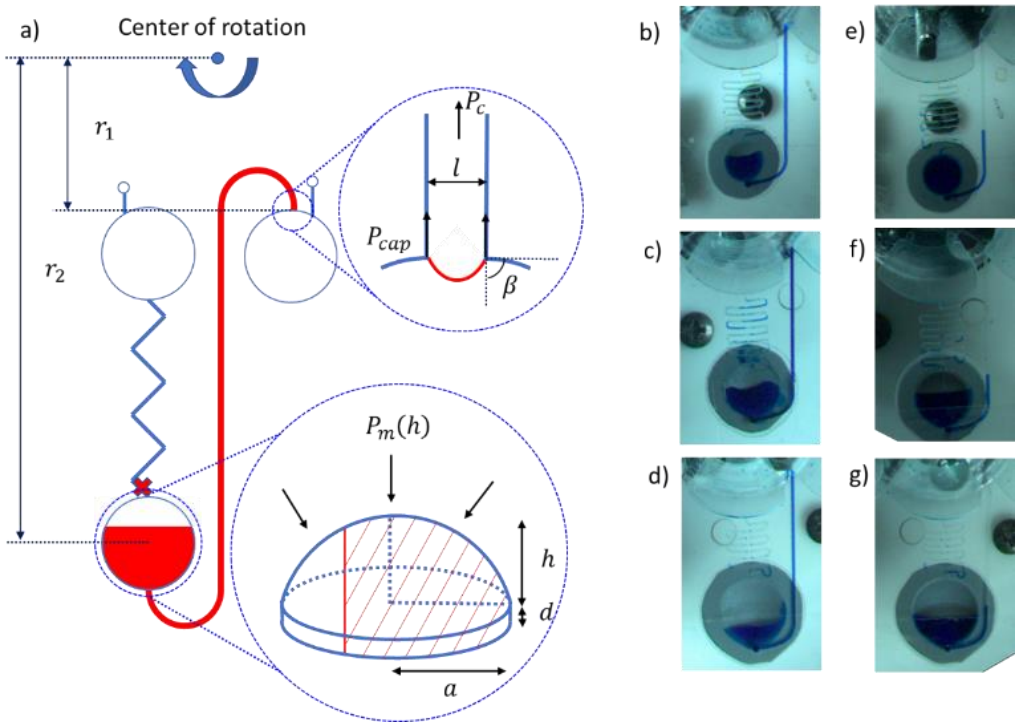

Figure 3.9. a) Schematic drawing related to the analysis of the liquid/membrane equilibrium of the spinning disc. In most cases, the recirculating chamber is partially filled as indicated by the shaded area. To simplify the calculation, we only discuss three situations: fully-filled, half-filled, and empty recirculation chamber. Here r_1 is the radial position of the exit of the recirculating channel, r_2 is the radial position of the center of the recirculating chamber, θ is the contact angle of water/ PMMA, l is the width and height of the recirculating channel with a square cross-sectional area, a is the radius of the recirculating chamber, h is the bulge height of the elastic membrane. The inlet channel was considered blocked, and the recirculating chamber was considered filled with liquid. b), c), d) are screenshots of the recirculating chamber with different radii at 180rpm after the tests. The

filling level of the recirculating chamber gets lower as the recirculating chamber gets larger. e), f), and g) are screenshots taken at the 3600-rpm period of the test. The volume of air trapped in the recirculating chamber gets larger as the chamber size is increased.

By substituting Eq. (3), (4), (6), and (7) into Eq. (5), we obtain Eq. (8):

$$C_1 \frac{Eth^3}{(1-\nu)a^4} + C_2 \frac{\sigma_0 th}{a^2} = \frac{1}{2}\rho\omega^2[((r_2 - a)^2 - r_1^2)] - \frac{3\sigma cos\theta_p^* + \sigma cos\theta_a}{4l} \quad \text{(Eq 3.8)}$$

As the elastic membrane was assembled with no initial stress, the value of σ_0 is 0. The equation can be simplified as follow:

$$C_1 \frac{Mth^3}{a^4} = \frac{1}{2}\rho\omega^2[((r_2 - a)^2 - r_1^2)] - \frac{3\sigma cos\theta_p^* + \sigma cos\theta_a}{4l} \quad \text{(Eq 3.9)}$$

To calculate the volume of the recirculating chamber, the bulge height was calculated:

$$h = \sqrt[3]{a^4(1-\nu) \times \frac{\frac{1}{2}\rho\omega^2[((r_2-a)^2-r_1^2)] - \frac{3\sigma cos\theta_p^* + \sigma cos\theta_a}{4l}}{C_1 Et}} \quad \text{(Eq 3.10)}$$

The volume of the recirculating chamber can be calculated using a hemispherical cap approximation and the volume of the original flat recirculating chamber:

$$V_{Re} = \frac{2}{3}\pi a^2 h \quad \text{(Eq 3.11)}$$

$$V_{Ori} = \pi a^2 d \quad \text{(Eq 3.12)}$$

Therefore, the maximum leftover volume $V_{leftmax}$ can be calculated from the following equation:

$$V_{leftmax} = V_{leftmax} = V_{Re} + V_{Ori} + V_{RC} = \frac{2}{3}\pi a^2 h + Ll^2 + \pi a^2 d \quad \text{(Eq 3.13)}$$

where L is the length of the recirculating channel and l is the width and height of the recirculating channel, d is the thickness of the bonding adhesive. The parameters used for the calculation are listed in Appendix B Table B5.

We also calculated the volumes when the recirculating chamber is half-filled with liquid or empty. The equations for each situation are:

Half-filled:

$$h = \sqrt[3]{a^4(1-\nu) \times \frac{\frac{1}{2}\rho\omega^2(r_2^2 - r_1^2) - \frac{3\sigma cos\theta_p^* + \sigma cos\theta_a}{4l}}{C_1 Et}} \quad \text{(Eq 3.14)}$$

$$V_{leftmax} = \frac{1}{3}\pi a^2 h + \frac{1}{2}\pi a^2 d + Ll^2 \quad \text{(Eq 3.15)}$$

Empty:

$$h = \sqrt[3]{a^4(1-\nu) \times \frac{\frac{1}{2}\rho\omega^2[((r_2+a)^2 - r_1^2)] - \frac{3\sigma cos\theta_p^* + \sigma cos\theta_a}{4l}}{C_1 Et}} \quad \text{(Eq 3.16)}$$

$$V_{leftmax} = Ll^2 \quad \text{(Eq 3.17)}$$

To compare the calculated result with the experimental result, the filling ratios of the recirculating chamber for average experimental results, η , were introduced here, which can be calculated by the following equation:

$$\alpha = \frac{V_{leftexp} - V_{RC}}{V_{Re} + V_{Ori}} = \frac{V_{leftexp} - Ll^2}{\frac{2}{3}\pi a^2 h + \pi a^2 d} \quad \text{(Eq 3.18)}$$

where $V_{leftexp}$ is the average experimental leftover volume. The calculated volumes and the average experimental volumes are shown in Table 3.1. The volumes for fully filled chambers and the volumes for empty chambers set the range of the possible leftover volume. As the chamber radius increases, the higher and lower limits of the possible leftover volume get larger. Meanwhile, the window for possible leftover volume gets bigger, which agrees with the trend in the experimental data. However, the filling ratio of the recirculating chamber gets smaller when the chamber size is increased, which has also been observed in experiments as shown in Figure 3.8b-d. The latter can be explained by the fact that during the high-rpm spin, the volume of the air trapped in the recirculating chamber becomes larger as the radius of the recirculating chamber gets bigger. The increase in trapped air volume contributes to a reduction in the filling ratio of the recirculating chamber as the chamber radius increases.

Table 3.1 Calculated leftover volumes with different radii and different filling conditions corresponding to different tested volumes. The tested volumes sit between the volume for fully filled chambers and the volume for empty chambers.

Radii of the recirculating chamber(mm)	Volumes for fully filled chamber (μl)	Volumes for half-filled chamber (μl)	Volumes for empty chamber (μl)	Average experimental volumes (μl)	Filling ratio of the recirculating chamber
3	22.10	15.61	8.51	17.36	65.11%
4	41.29	26.09	8.72	19.93	34.42%
5	73.62	44.14	8.96	23.34	22.24%

In general, to obtain a higher inward pumping efficiency for a specific amount of initial volume, a smaller chamber is desired as it has a smaller leftover volume. As a trade-off, the smaller chamber holds a smaller amount of liquid, leading to a limited amount of liquid pumped for each cycle. Therefore, a smaller chamber requires more cycles to complete the inward pumping when a large initial volume is loaded. Another concern for the small

recirculating chamber is that with a large initial volume, the pressure generated during high speed can cause the deterioration of the elastic membrane and delamination of the adhesives. Therefore, the chamber diameter should be designed according to the initial volume and desired inward pumping efficiency.

3.4.2 Blood/plasma fluidic unit integrated with inward pumping mechanism

One of the most widely used point-of-care testing sample preparation steps is the blood/plasma separation, which is usually the first step of most blood-related biological assays. However, when implemented on a centrifugal microfluidic disc, the features need to be located at the edge of the CD to fully utilize the centrifugal force[45]. Without any inward pumping approaches, the CD has to be larger to accommodate any other steps. As an example application for the mechanism, we designed, fabricated, and tested a bpsCD with 150 µl bovine blood, as shown in Figure 3.4c. A schematic drawing of the working principle and results are shown in Figure 3.10. The design had a small channel connecting the recirculating chamber and the 75 µl blood cell chamber, preventing the backflow of red blood cells during deceleration. After being separated from the blood, the remaining 75 µl of plasma was transferred to the collection chamber through the same cycles as in the inward pumping efficiency tests. The calculated inward pumping efficiency for plasma was 86% higher than for the DI water with an even higher initial volume. This was mainly because during step 2, blood was transferred under high spin speed and started to separate in the trenches and bends of the inlet channel. As shown in the red circle in Figure 3.10c, the blood cells sedimented blocked the inlet channel, further increasing resistance for plasma to flow inwards through the inlet channel. As a result, the recirculating channel

became the only outlet out of the recirculation chamber. Therefore, the leftover liquid in this test was less than in the quantification test performed with DI water, providing a higher transfer efficiency.

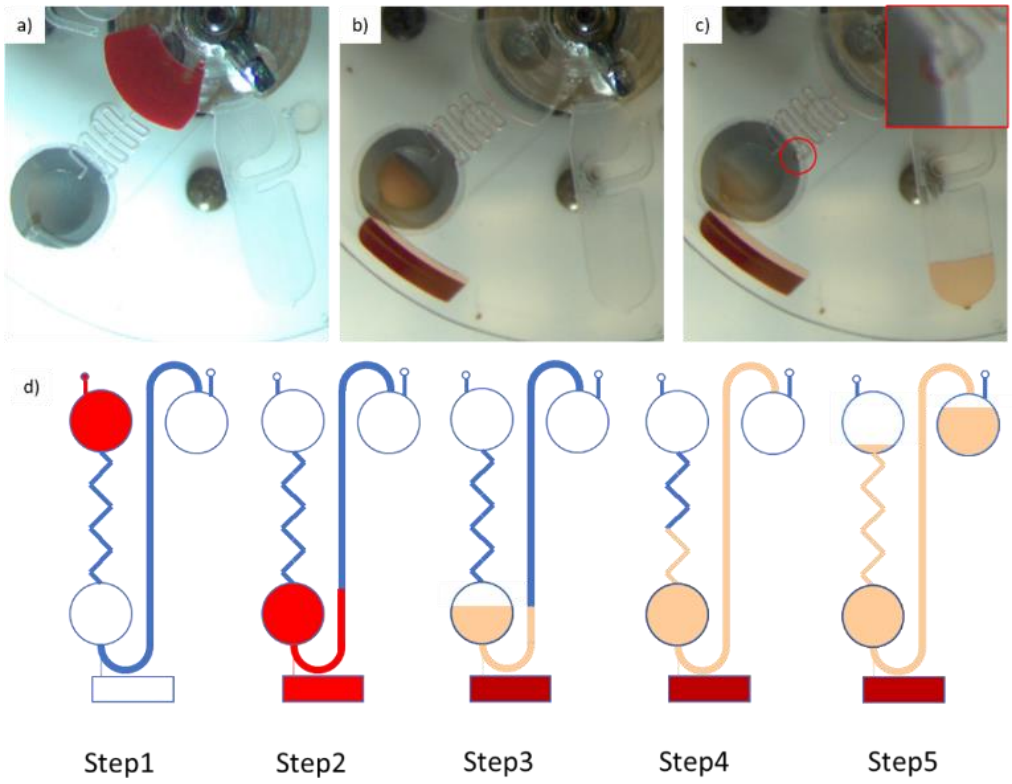

Figure 3.10. Blood/plasma separation and inward pumping were achieved using the bpsCD. a) Loading 150µl bovine blood into the loading chamber. b) Blood/plasma separation at 4500 rpm. c) Through multiple cycles, the plasma was transferred to the collection chamber. The red circle indicates the region where the red blood cells sediment in the channel. The insert is the enlarged picture of the red circle for clarity. d) A schematic drawing of the blood/plasma separation test.

3.4.3 Recirculation/mixing capabilities

In microfluidic systems, reagent rehydration and hybridization of biomolecules often require fluidic systems to have appropriate mixing capabilities to achieve reliable results within a short timeframe[70]. To evaluate the mixing capability of the inward pumping mechanism, experiments were conducted with the design shown in Figure 3.4b, and the

spin profile is shown in figure 3.4e. Screenshots were made, as shown in Figure 3.11a-f. It can be seen from Figure 3.11d and Figure 3.11f that most of the liquid that was pumped inwards traveled through the recirculating channel, as the inlet channel remains partially filled. These screenshots were processed with ImageJ to split into red, green, and blue channels for ease of measurement. Histograms for the blue channel were taken and shown next to the corresponding screenshots to evaluate the mixing efficiency. The center of the disc was selected as the sampling area for ease of assessment. The standard deviations of the pixel intensity in the blue channel were used as mixing indexes to evaluate the mixing efficiency[72]. As shown in the histograms, the standard deviations got smaller as the test went on, reaching a value of 6.439 at the end of the second cycle. As the test continued, the standard deviation remained around 6.5, indicating that mixing was complete.

As the fluidic mixing happened during the fast deceleration step shown in Figure 3.11c, we hypothesize that the mixing was a result of the elongation of the laminar fluidic interface due to the Euler force. As the Euler force is linearly dependent on the radial position, the liquid in the recirculating chamber features an Euler force gradient in the radial direction, leading to a vortex forming in the chamber, as shown in Figure 3.11c. This vortex folds the layers of fluid together and thus minimizes the diffusion length and greatly enhances mixing and homogenization, which is consistent with other results from the literature and is especially important when operating in the laminar fluidic regime (as seen in Appendix B) [112]. At the same time, the liquid was pumped inwards through the recirculating channel without being mixed by the vortex. This portion of liquid could only join the mixing event after the second 3600 rpm step, shown in Figure 3.11e. Therefore, a minimum of two

cycles is required to complete the mixing. Besides, this recirculation design created a circular fluidic route that allowed the liquid to flow in one way in the channels (radially inwards through the recirculating channel and radially outwards through the inlet channel), ensuring a faster mixing. It is essential for reagent rehydration, where the liquid with a longer residence time with the dried reagent usually has a higher reagent concentration than the liquid with a shorter residence time[57,70]. Another potential application is for accelerating diffusion-limited reactions, where the liquid usually generates a depletion region when it flows through the reaction area[107]. This mechanism reduces the depletion region by mixing the liquid which has flowed through the reaction region, with the liquid that has not, which is still abundant in reactive species. With thorough mixing and inward pumping capabilities, this recirculation mechanism has great potential in facilitating hybridization events in biological assays.

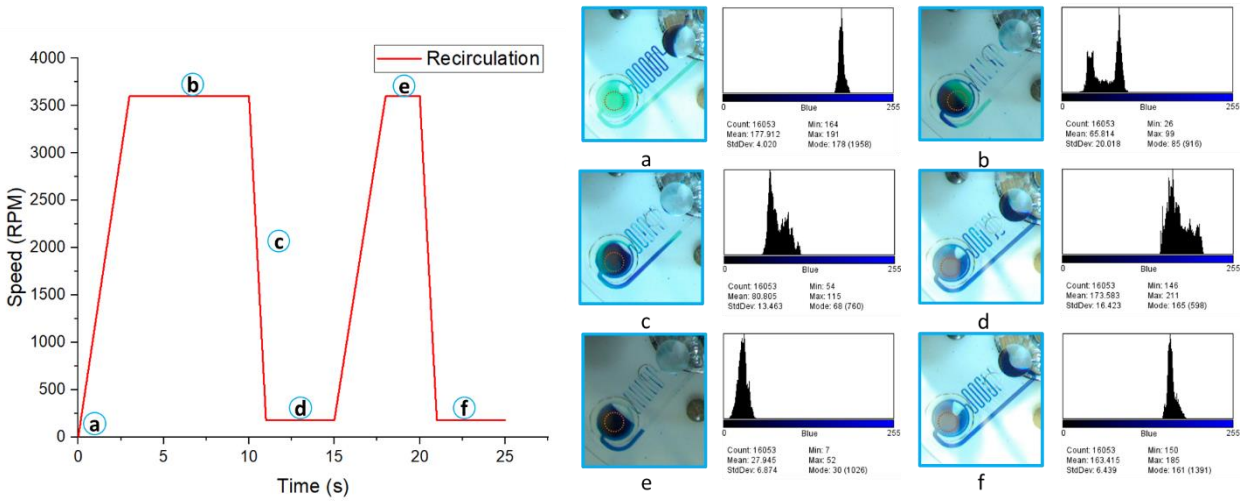

Figure 3.11. The recirculation and mixing efficiency test. As shown in the screenshots a)-f), the liquid was moved in a circular pattern, with no liquid returning to the loading chamber through the inlet channels. The histograms of the color intensity inside the circled area in the recirculating chamber are shown next to the corresponding screenshots, indicating the mixing was completed during the second cycle.

3.4.4 Hybridization tests for various fluidic profiles

Preliminary hybridization tests were conducted with 3 different designs and 2 protocols shown in Figure 3.5 and Appendix B Table B4. The design that uses an elastic membrane for recirculation has a high failure rate due to the delamination of the elastic membrane. It should be noted that compared to the inward pumping or plasma separation tests which were conducted in less than 10 minutes, the time of the hybridization tests is 40 mins. Nevertheless, the results of the other two tests, recirculation with ventless chamber and reciprocation with ventless chamber are shown in Figure 3.12. It can be told from the figures that both recirculation and reciprocation showed a sufficient binding. However, the spots in the reciprocation test were blurred and had tails that connect with other spots. This phenomenon causes problems in signal interpretation, making it harder to determine the contour of spots. As shown in the insert in Figure 12d, the tailed shape of spots sometimes enlarges the spot contours or even connects neighboring spots, causing a lower average pixel intensity. It is further verified by the signal intensity comparison results shown in Table 3.2, which were obtained using the image processing code we mentioned in Chapter 2. The coefficient of variant is calculated by Equation 3.19:

$$CV = \frac{Std}{\bar{I}} \times 100\% \qquad \text{(Eq 3.19)}$$

where $\bar{I}$ is the mean value of mean pixel intensities of different spot contours, and Std is the standard deviation of mean pixel intensity of different spot contours. It shows that the recirculation not only has a higher signal but also is spatially more consistent in terms of

spot locations. Nevertheless, this study shows a promising direction to improve the enhancement of assay performance via recirculation mechanisms.

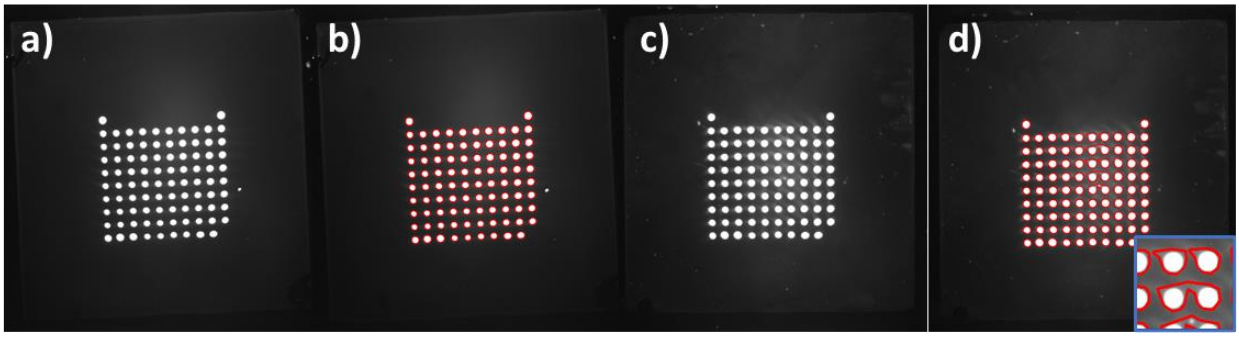

Figure 3.12. The hybridization test result for a) recirculation with ventless chamber, and c) reciprocation with ventless chamber. Using the code provided in Chapter 2, we can find the contours of the spots shown in b) and d) using computer algorithms. It shows that the blurred spots for reciprocation can cause trouble for image analysis by enlarging the spot area and connecting neighboring spots.

Table 3.2. Pixel intensity calculation of hybridization result comparing recirculation and reciprocation.

	Reciprocation	Recirculation
Mean intensity of different spots (grayscale)	203.94	206.04
Standard deviation	5.21	2.31
Coefficient of variant (%)	2.55	1.12

3.5 Summary

In this chapter, we demonstrated a novel recirculation mechanism for liquid manipulation on the centrifugal microfluidic platform that requires no external equipment. This mechanism uses an elastic membrane to store and release energy. Through multiple cycles, liquid can be recollected at the center of the CD through a recirculating channel. Inward pumping efficiency tests were carried out to evaluate the fluid transfer mechanism. An

inward pumping efficiency of over 78% was achieved with various initial volumes and recirculating chamber designs. An analysis that used conservative assumptions was conducted to estimate the range of leftover volume for the recirculating chamber with different sizes. Recirculation and mixing tests were also conducted to explore the potential applications of this fluid transfer mechanism, demonstrating its mixing capability and the unique ability to move liquid in a circular fluidic route. A design that combined this mechanism with blood/plasma separation was also fabricated and tested with bovine blood, indicating a plasma pumping efficiency of 86%. Preliminary tests to compare the different fluidical influences on the hybridization process were conducted, showing a promising direction for performance enhancement via recirculation mechanism. These results showed a tunable recirculation mechanism on the centrifugal microfluidic platform with high efficiency and unique liquid movement capabilities as a powerful tool in fluidic manipulation and improvement for assay performance. However, the hybridization results were obtained by the recirculation with ventless chamber design. Compared to the elastic-membrane-enabled recirculation, the ventless chamber design still has a dead volume that stays in the ventless chamber and requires large real estate on the CD. When it comes to larger sample volume, the ventless chamber design needs a higher spin speed to drain the solution from the microarray surface, which imposes more restrictions on the motor. Therefore, the elastic-membrane-enabled recirculation is still worth exploring. Future directions could foucus on material selection and fabrication process optimization.

Chapter 4

Implementation of phenotypic antibiotic susceptibility test

In this chapter, we used the centrifugal microfluidic platform described in Chapter 2 to perform a phenotypic antibiotic susceptibility test. We selected an rRNA-based AST that detects the rRNA copies of bacteria [97]. As the species-specific rRNAs are abundant in bacteria during their self-replication and are highly susceptible to the presence of antibiotics, they can serve as ideal identifiers for bacteria and indicators for antibiotic susceptibility. The detailed steps of the assay are shown in Appendix C table C1.

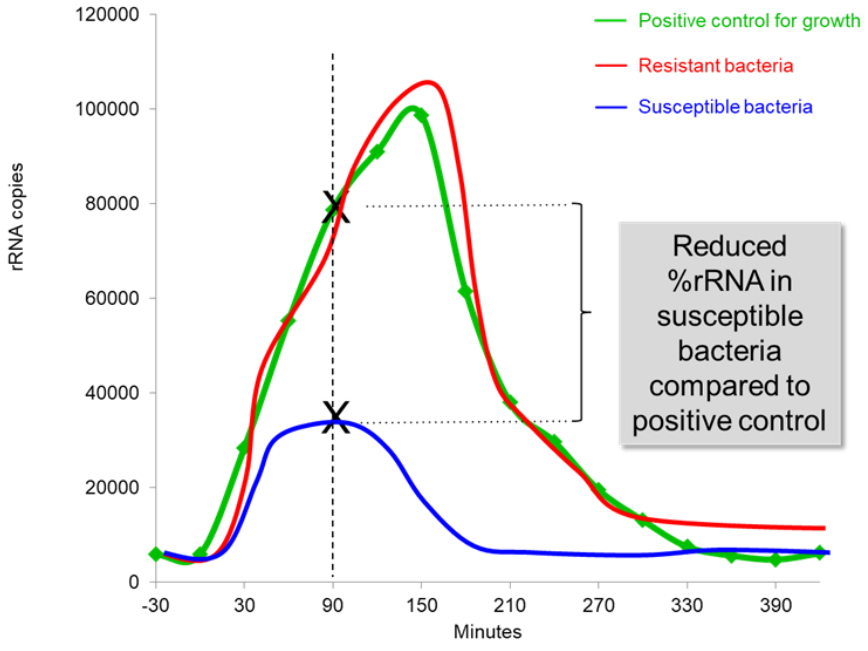

Figure 4.1 rRNA as an ideal indicator for bacteria growths and antibiotic susceptibility. Reprinted from [97].

4.1 Materials and methods

The CD platform construction and the materials used in the tests were discussed in Chapter 2. In this section, we will describe the CD used for the AST test and the corresponding protocol for the SpinBox.

4.1.1 CD design and fluidic steps

Based on the assay steps, we design and fabricated the CD shown in Figure 2.2b. For automation of the ASTs, we preloaded the CD with lyophilized reagents as shown in Figure 4.2.

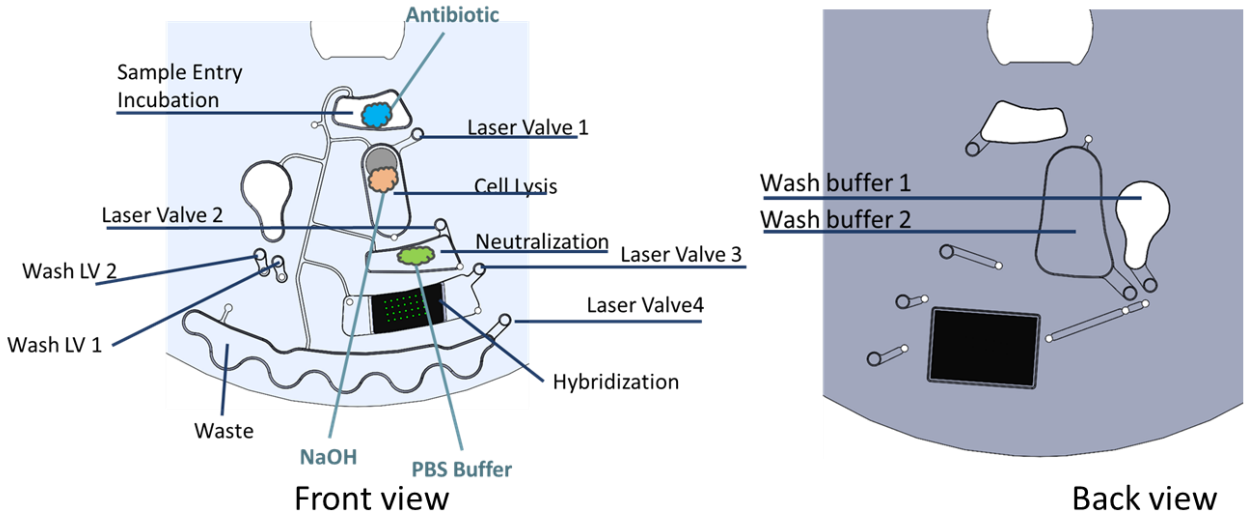

Figure 4.2 The detailed view of the CD design for ASTs. Reagents are preloaded in different chambers for different assay steps.

An oscillation protocol is used to incubate bacteria once in the incubation chamber (Figure 4.3). The incubation chamber is subject to cycles of rapid acceleration/deceleration to generate vigorous mixing. The robust mixing provides even distribution of macromolecules (e.g., antibiotics and nutrients) and ensures sufficient sample aeration, required for

bacterial growth. Oscillation is also used in the neutralization chamber to resuspend the dried-down phosphate buffer.

The lysis chamber utilizes a combination of mechanical and chemical lysis to effectively release genomic data from a number of bacterial pathogens. As the microfluidic disc is rotated at a low angular velocity (<500 RPM), the metal disc interacts with the array of permanent magnets, moving back and forth in the lysis chamber and mixing the sample with the silica-zirconia beads and the chemical lysis reagent (1 M NaOH). The mechanical forces generated between the metal disc and beads provide shear forces that break open cell walls.

The neutralization chamber contains dried-down PBS and fluorescently labeled detector probes, which are resuspended during oscillation of the disc. The PBS neutralizes the NaOH from the lysis chamber, preventing degradation of rRNA sequences. At this point, the sample can be either removed from the disc, for detection on a separate system (e.g., Luminex Mag-Pix or other fluorescent microscopes), or can continue for hybridization and detection directly in the disc if a microarray is inserted into the detection chamber.

The hybridization and detection chamber contains a sticky adhesive on one side, allowing a glass or polymer slide functionalized with detector probes (microarray) to snap into the back of the disc. A 9 x 5 mm window exposes the detector probes to the rest of the chamber. Following neutralization, neutralized lysate slowly fills up the chamber. Diffusion, combined with oscillatory mixing, allows rRNA to hybridize and bind with the complementary detector probes. Following hybridization, two wash buffers are released, flowing through the chamber to wash away any unbound rRNA into a waste chamber,

eliminating false-positive results. After these washing steps, the detection chamber is imaged using the camera and fluorescent lenses present in the SpinBox. The flow of liquid is shown in Figure 4.3, which is controlled by the laser valves that we described in Chapter 2. The spin protocol of the test is described in Appendix C Table C2.

To demonstrate our system was efficient in determining antibiotic susceptibility, 11 different *E. coli* isolates were incubated with a total of five commonly prescribed, broad-spectrum antibiotics using the microfluidic disc and compared to the 96-well plate. We chose three antibiotics whose mechanism of action inhibits the bacterial cell wall (ampicillin, cefazolin, and ceftriaxone) and two antibiotics that target bacteria DNA functions, thereby preventing replication (nitrofurantoin and ciprofloxacin).

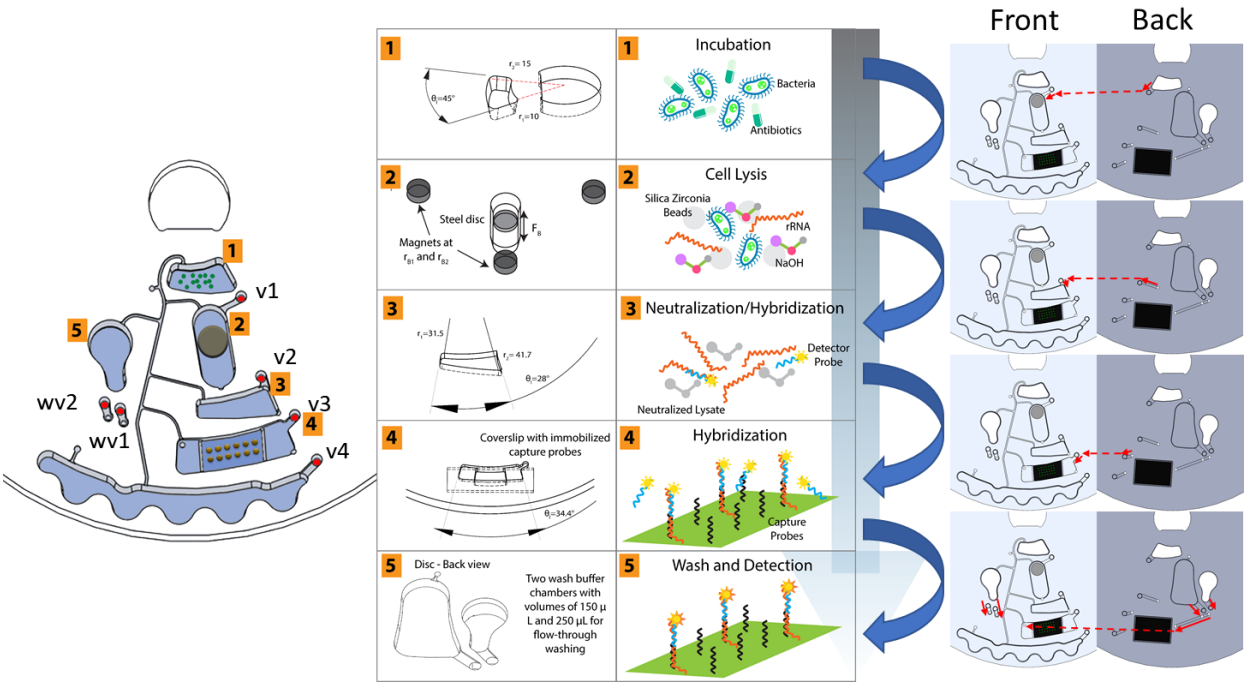

Figure 4.3 The microfluidic disc design is shown with assay steps on right corresponding to fluidic chambers labeled on the disc. The middle column highlights critical features of important fluidic geometries on the disc. The red arrows in the right column indicate the flow sequence of liquid.

4.2 Result and discussion

The ratios of the signals are used to determine antibiotic susceptibility. It is calculated by comparing the signal from the bacteria incubated with antibiotics to the positive control, where the same bacteria are incubated without antibiotics. If the ratio is large (near or above 1), the bacteria are resistant since their growth is similar to the no antibiotic control. *Vice versa*, If the ratio is small (closer to or below 0), the bacteria are susceptible since their growth is suppressed by the antibiotic and much less than the no antibiotic control. Figure 4.4 shows the ratio from the rRNA signals of bacteria incubated with and without antibiotics (Abx/No Abx) for both the disc (Figure 4.4a) and the plate (Figure 4.4b). The red and blue lines in Figure 11 show the average of all resistant or susceptible bacteria on either the disc or plate (error shown as a gradient). While both the plate and the disc showed significant differences in average ratios between the resistant and susceptible bacteria ($p<0.01$), the resistant bacteria showed higher average ratios on the disc than the plate ($p<0.05$) indicating an improved ability to distinguish antibiotic susceptibility on the disc.

In Figure 4.5, an average ratio for the response of multiple bacteria to each antibiotic was calculated. In all bacteria/antibiotic combinations, the average ratios from the disc incubation were comparable to those on the 96-well plate. However, on the disc, susceptible bacteria incubated with antibiotics showed very low uniform average ratios, with no statistically significant differences between antibiotic effectiveness. Interestingly, on the plate, susceptible bacteria exposed to the three antibiotics that target the cell wall (ampicillin, cefazolin, and ceftriaxone), showed a lower average ratio than those exposed to antibiotics that target bacterial DNA functions (nitrofurantoin and ciprofloxacin) (<0.05). This uncertainty could contribute to false positives when interpreting susceptibility data.

Therefore, results from the disc incubation provide clinicians with more confidence in their prescription of antibiotics.

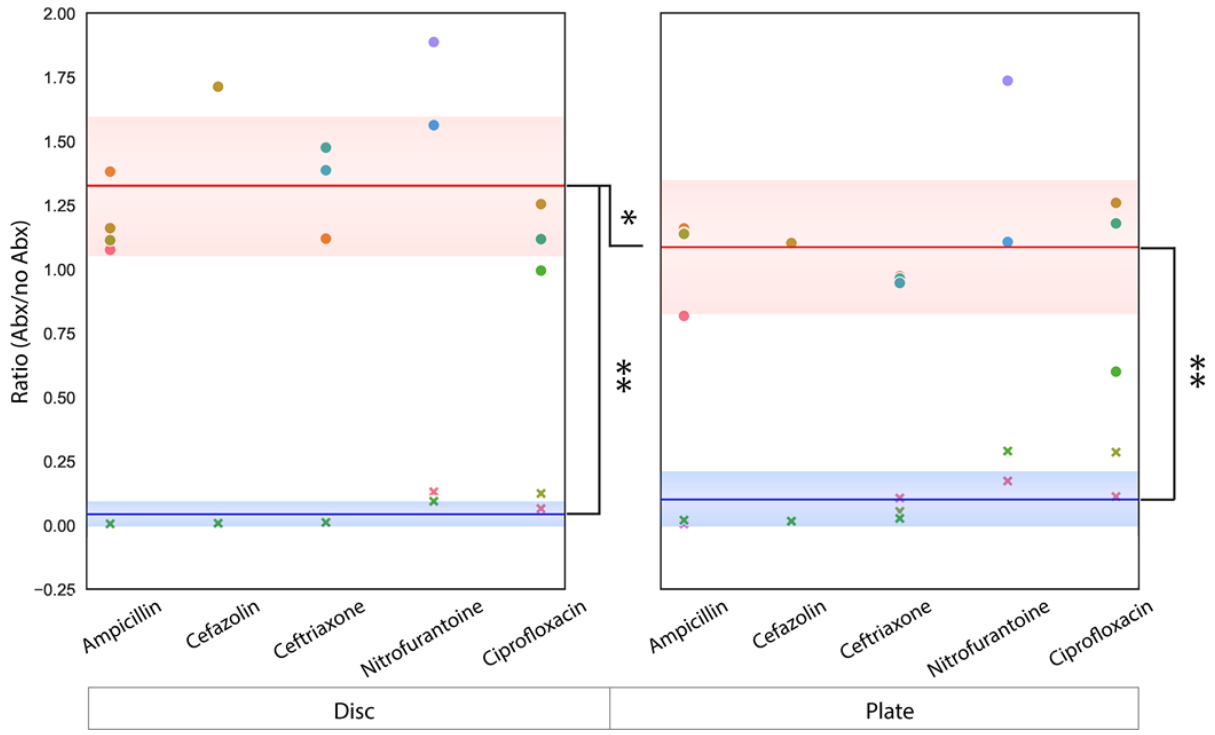

Figure 4.4 Ratios of signal intensity of each isolate of bacteria incubated with and without antibiotics for the disc (a) and the plate (b). The blue and red lines represent the average of all ratios for resistant (red) and susceptible (blue) bacteria.

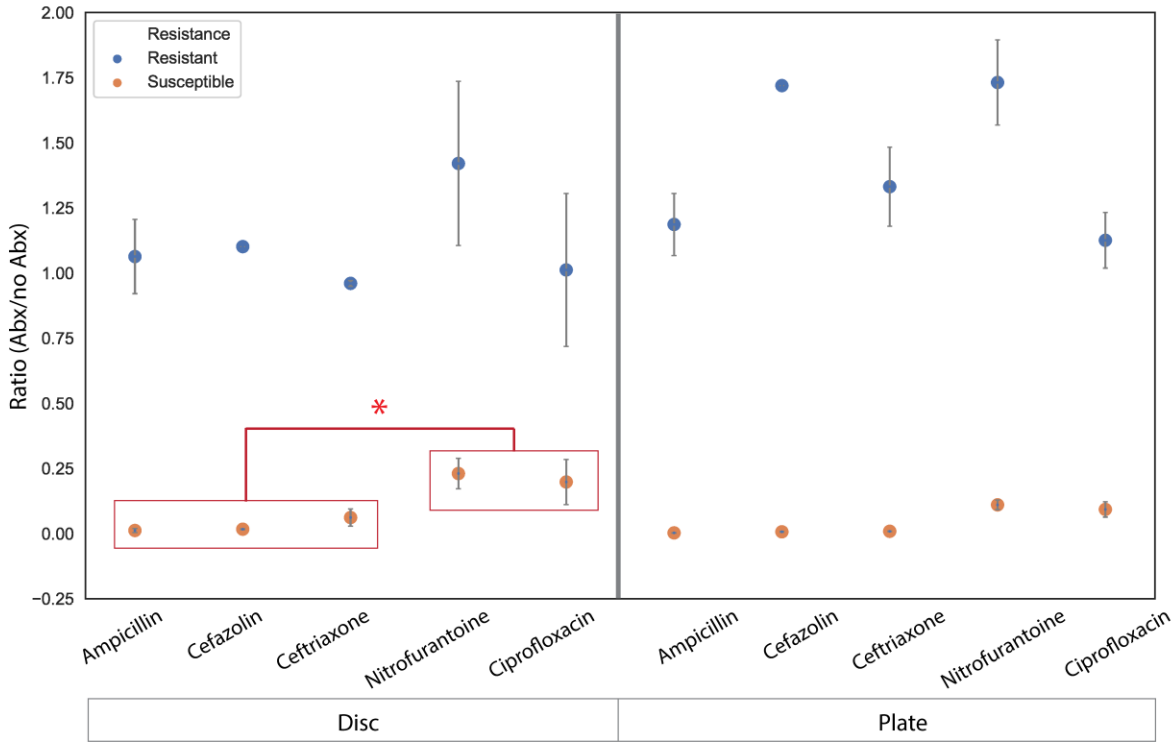

Figure 4.5 Average ratio of signal intensity of *E. coli* strains incubated with and without each antibiotic. The graph on the right shows the ratios for resistant and susceptible bacteria grown on the plate and the left shows resistant and susceptible bacteria grown on the disc.

4.3 Summary

In this chapter, we successfully demonstrated the automation of a phenotypic AST on the centrifugal microfluidic system. The injection-molded CDs and the custom-designed SpinBox can automate all sample processing steps of the rRNA-based AST, with similar or even higher performance compared to a benchtop assay. The system serves as a powerful step towards improving rapid AST PoC diagnostics by minimizing sample handling.

Chapter 5

Conclusion and Outlook

In this thesis, I first described the development of the centrifugal microfluidic platform as a versatile platform for biological assay sample preparation in Chapter 2. This system has shown a powerful incubation capability compared with the conventional method that uses 96-well plates in plate shaker incubators. With a laser valving unit, the fluidic control is achieved with high precision. Lysis for gram-positive and gram-negative bacteria was achieved with the chemical mechanical lysis to release genomic data.

In Chapter 3, a recirculation mechanism was described for inward pumping, thoroughly mixing, and potential enhancement for hybridization. I performed a parametric study to provide engineering control of the mechanism and used calculations to theoretically predict the pumping efficiency of the inward pumping efficiency. I also implemented a blood/plasma separation step for this mechanism, providing a potential application.

Hybridization tests of microarray were conducted to investigate the influence of reciprocation and recirculation, providing a promising approach to enhance hybridization efficiency via recirculation mechanism.

In Chapter 4, I described the use of the centrifugal microfluidic platform for bacteria study. A phenotypic AST was automated on the instrument we developed, showing the ability to rapidly identify resistance in 11 different *E. Coli* isolates in 2 hours. It should be noted that in this study, we used bacteria isolates to validate the test. However, in clinical settings,

patient samples are mostly polymicrobial, which utilized the multiplexing feature of microarrays.

To be noted, this work covers a wide range of fields including microbiology, centrifugal microfluidics, system integration, and molecular biology, which can never be done by one person alone. I participated in the work presented in this thesis and contributed as a leading effort in system building, software programming, recirculation study, and CD cartridge design for AST.

Beyond the scope of this work, there are many unexplored aspects of this work that I would pursue in my future work or inspire the work from other researchers in this multidisciplinary field.

1. As I demonstrated, the recirculation mechanism can perform hybridization for assays involving microarrays. However, the science behind this mechanism is not yet understood and parameters could be further optimized. Although the hybridization results were obtained by the recirculation with ventless chamber design. Compared to the elastic-membrane-enabled recirculation, the ventless chamber design still has a dead volume that stays in the ventless chamber and requires large real estate on the CD. Moreover, when it comes to larger sample volume, the ventless chamber design needs a higher spin speed to drain the solution from the microarray surface, which imposes restrictions on the motor. Therefore, the elastic-membrane-enabled recirculation is still worth exploring.
2. For the elastic-membrane-enabled recirculation mechanism, a critical unsolved issue lies in the manufacturing process. The thin elastic membrane inserts are

difficult to be handled either manually or with pick and place robotic arms. The use of adhesive for bonding further complicates the fabrication process. Potential solutions include using elastic membranes with the size same as the CD (as shown in Figure 5.1) and replacing the adhesive bonding with ultrasonic welding. Other concerns regarding the fragility of using elastic membrane occurred during the hybridization test, as the recirculation with elastic membrane design delaminated under long experimental time. This could also be a future direction to improve the robustness of elastic membrane involved centrifugal microfluidic system [65,66].

3. Due to the time constraints, we only demonstrate the phenotypic AST on the CD platform that we developed with fluorescent detection. Other biological assays that involve fluorescent detection and other detection mechanisms such as electrochemical detection, chemiluminescence, and absorbance spectroscopy can also be implemented with some modification to the system. Another improvement that could be made is the miniaturization of the device to make it more suitable for point of care diagnostics, or extreme point of care diagnostics, where reliable power is limited.

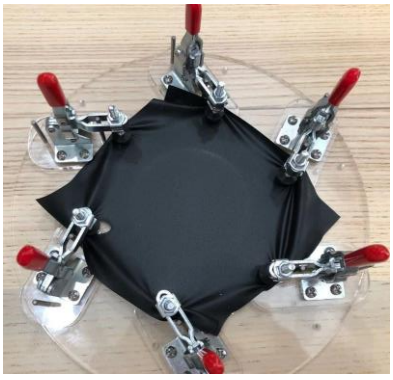

Figure 5.1 A membrane holder for CD assembly that uses elastic membranes with the size same as the CD.

Bibliography

1. Inhorn, M.C.; Brown, P.J. The Anthropology of Infectious Disease. *Annu. Rev. Anthropol.* **1990**, *19*, 89–117, doi:10.1146/ANNUREV.AN.19.100190.000513.

2. Diamond, J.M. Guns, germs, and steel : The fates of human societies. **1997**, 480.

3. McMichael, A.J. Globalization, Climate Change, and Human Health. *N. Engl. J. Med.* **2013**, *368*, 1335–1343, doi:10.1056/NEJMRA1109341/SUPPL_FILE/NEJMRA1109341_DISCLOSURES.PDF.

4. WHO Coronavirus (COVID-19) Dashboard | WHO Coronavirus (COVID-19) Dashboard With Vaccination Data Available online: https://covid19.who.int/ (accessed on Feb 4, 2022).

5. Fair, R.J.; Tor, Y. Antibiotics and Bacterial Resistance in the 21st Century. *Perspect. Medicin. Chem.* **2014**, *6*, 25, doi:10.4137/PMC.S14459.

6. Sehgal, M.; Ladd, H.J.; Totapally, B. Trends in Epidemiology and Microbiology of Severe Sepsis and Septic Shock in Children. *Hosp. Pediatr.* **2020**, *10*, 1021–1030, doi:10.1542/HPEDS.2020-0174.

7. Coates, A.R.; Halls, G.; Hu, Y. Novel classes of antibiotics or more of the same? *Br. J. Pharmacol.* **2011**, *163*, 184–194, doi:10.1111/J.1476-5381.2011.01250.X.

8. Silver, L.L. Challenges of antibacterial discovery. *Clin. Microbiol. Rev.* **2011**, *24*, 71–109, doi:10.1128/CMR.00030-10/ASSET/3D6620EB-B423-46C8-A546-

F98C7C29FE73/ASSETS/GRAPHIC/ZCM9990923370008.JPEG.

9. Health matters: antimicrobial resistance - GOV.UK Available online: https://www.gov.uk/government/publications/health-matters-antimicrobial-resistance/health-matters-antimicrobial-resistance (accessed on Feb 4, 2022).

10. World Health Organization *The International Health Regulations (2005) Third Edition*; 2016; ISBN 978 92 4 158049 6.

11. Li, Y.; Yan, X.; Feng, X.; Wang, J.; Du, W.; Wang, Y.; Chen, P.; Xiong, L.; Liu, B.F. Agarose-based microfluidic device for point-of-care concentration and detection of pathogen. *Anal. Chem.* **2014**, *86*, 10653–10659, doi:10.1021/AC5026623/SUPPL_FILE/AC5026623_SI_004.AVI.

12. Jorgensen, J.H.; Ferraro, M.J. Antimicrobial susceptibility testing: A review of general principles and contemporary practices. *Clin. Infect. Dis.* **2009**, *49*, 1749–1755, doi:10.1086/647952/2/49-11-1749-FIG003.GIF.

13. Peeling, R.W.; Holmes, K.K.; Mabey, D. Rapid diagnostic tests for sexually transmitted infections. **2006**, doi:10.1136/sti.2006.024265.

14. van Belkum, A.; Bachmann, T.T.; Lüdke, G.; Lisby, J.G.; Kahlmeter, G.; Mohess, A.; Becker, K.; Hays, J.P.; Woodford, N.; Mitsakakis, K.; et al. Developmental roadmap for antimicrobial susceptibility testing systems. *Nat. Rev. Microbiol. 2018 171* **2018**, *17*, 51–62, doi:10.1038/s41579-018-0098-9.

15. Ross, J.I.; Snelling, A.M.; Eady, E.A.; Cove, J.H.; Cunliffe, W.J.; Leyden, J.J.; Collignon, P.;

Dréno, B.; Reynaud, A.; Fluhr, J.; et al. Phenotypic and genotypic characterization of antibiotic-resistant Propionibacterium acnes isolated from acne patients attending dermatology clinics in Europe, the U.S.A., Japan and Australia. *Br. J. Dermatol.* **2001**, *144*, 339–346, doi:10.1046/J.1365-2133.2001.03956.X.

16. Campbell, J.; McBeth, C.; Kalashnikov, M.; Boardman, A.K.; Sharon, A.; Sauer-Budge, A.F. Microfluidic advances in phenotypic antibiotic susceptibility testing. *Biomed. Microdevices* **2016**, *18*, 1–11, doi:10.1007/S10544-016-0121-8/FIGURES/3.

17. Hol, F.J.H.; Dekker, C. Zooming in to see the bigger picture: Microfluidic and nanofabrication tools to study bacteria. *Science (80-.).* **2014**, *346*, doi:10.1126/SCIENCE.1251821/ASSET/ADABEAE4-D5D9-44E2-8A32-6E907C37393C/ASSETS/GRAPHIC/346_1251821_F4.JPEG.

18. Jang, S.; Lee, B.; Jeong, H.H.; Jin, S.H.; Jang, S.; Kim, S.G.; Jung, G.Y.; Lee, C.S. On-chip analysis, indexing and screening for chemical producing bacteria in a microfluidic static droplet array. *Lab Chip* **2016**, *16*, 1909–1916, doi:10.1039/C6LC00118A.

19. Tan, S.J.; Kee, M.Z.L.; Mathuru, A.S.; Burkholder, W.F.; Jesuthasan, S.J. A Microfluidic Device to Sort Cells Based on Dynamic Response to a Stimulus. *PLoS One* **2013**, *8*, e78261, doi:10.1371/JOURNAL.PONE.0078261.

20. Mohan, R.; Sanpitakseree, C.; Desai, A. V.; Sevgen, S.E.; Schroeder, C.M.; Kenis, P.J.A. A microfluidic approach to study the effect of bacterial interactions on antimicrobial susceptibility in polymicrobial cultures. *RSC Adv.* **2015**, *5*, 35211–35223, doi:10.1039/C5RA04092B.

21. Liu, Z.; Sun, H.; Ren, K. A Multiplexed, Gradient-Based, Full-Hydrogel Microfluidic Platform for Rapid, High-Throughput Antimicrobial Susceptibility Testing. *Chempluschem* **2017**, *82*, 792–801, doi:10.1002/CPLU.201600654.

22. Aldridge, B.B.; Fernandez-Suarez, M.; Heller, D.; Ambravaneswaran, V.; Irimia, D.; Toner, M.; Fortune, S.M. Asymmetry and aging of mycobacterial cells lead to variable growth and antibiotic susceptibility. *Science (80-.).* **2012**, *335*, 100–104, doi:10.1126/SCIENCE.1216166/SUPPL_FILE/ALDRIDGE.SOM.PDF.

23. Liu, Z.; Banaei, N.; Ren, K. Microfluidics for Combating Antimicrobial Resistance. *Trends Biotechnol.* **2017**, *35*, 1129–1139, doi:10.1016/J.TIBTECH.2017.07.008.

24. Li, H.; Torab, P.; Mach, K.E.; Surrette, C.; England, M.R.; Craft, D.W.; Thomas, N.J.; Liao, J.C.; Puleo, C.; Wong, P.K. Adaptable microfluidic system for single-cell pathogen classification and antimicrobial susceptibility testing. *Proc. Natl. Acad. Sci. U. S. A.* **2019**, *116*, 10270–10279, doi:10.1073/PNAS.1819569116/-/DCSUPPLEMENTAL.

25. Haeberle, S.; Zengerle, R. Microfluidic platforms for lab-on-a-chip applications. *Lab Chip* **2007**, *7*, 1094–1110, doi:10.1039/B706364B.

26. Chin, C.D.; Linder, V.; Sia, S.K. Lab-on-a-chip devices for global health: Past studies and future opportunities. *Lab Chip* **2006**, *7*, 41–57, doi:10.1039/B611455E.

27. Tang, M.; Wang, G.; Kong, S.-K.; Ho, H.-P. A Review of Biomedical Centrifugal Microfluidic Platforms. *Micromachines* **2016**, *7*, 26.

28. Madou, M.; Zoval, J.; Jia, G.; Kido, H.; Kim, J.; Kim, N. Lab on a CD. *Annu. Rev. Biomed.*

Eng. **2006**, *8*, 601–628, doi:10.1146/annurev.bioeng.8.061505.095758.

29. Smith, S.; Mager, D.; Perebikovsky, A.; Shamloo, E.; Kinahan, D.; Mishra, R.; Torres Delgado, S.M.; Kido, H.; Saha, S.; Ducrée, J.; et al. CD-Based Microfluidics for Primary Care in Extreme Point-of-Care Settings. *Micromachines 2016, Vol. 7, Page 22* **2016**, *7*, 22, doi:10.3390/MI7020022.

30. Strohmeier, O.; Keller, M.; Schwemmer, F.; Zehnle, S.; Mark, D.; Von Stetten, F.; Zengerle, R.; Paust, N. Centrifugal microfluidic platforms: advanced unit operations and applications. *Chem. Soc. Rev.* **2015**, *44*, 6187–6229, doi:10.1039/c4cs00371c.

31. Gilmore, J.; Islam, M.; Martinez-Duarte, R. Challenges in the use of compact disc-based centrifugal microfluidics for healthcare diagnostics at the extreme point of care. *Micromachines* **2016**, *7*, doi:10.3390/mi7040052.

32. Burger, R.; Kirby, D.; Glynn, M.; Nwankire, C.; O'Sullivan, M.; Siegrist, J.; Kinahan, D.; Aguirre, G.; Kijanka, G.; Gorkin, R.A.; et al. Centrifugal microfluidics for cell analysis. *Curr. Opin. Chem. Biol.* **2012**, *16*, 409–414, doi:10.1016/j.cbpa.2012.06.002.

33. Perebikovsky, A. Engineered MEMS microenvironments for studying stem cells and microorganisms.

34. Piccolo Xpress | Abbott Point of Care Available online: https://www.globalpointofcare.abbott/en/product-details/apoc/piccolo-xpress-chemistry-analyzer.html (accessed on Feb 5, 2022).

35. Nexus IB10 | Nexus-Dx Available online: https://www.nexus-dx.com/nexus-ib10/

(accessed on Feb 5, 2022).

36. Revogene® | Meridian Bioscience Available online: https://www.meridianbioscience.com/diagnostics/platforms/molecular/revogene/ (accessed on Feb 5, 2022).

37. WaterLink Spin Touch | Code 3580, Code 3581, Code 3582 Available online: https://lamotte.com/waterlink-spin-touch (accessed on Feb 5, 2022).

38. Products - Spindiag Available online: https://www.spindiag.de/sars-cov-2-disk/ (accessed on Feb 5, 2022).

39. Gyrolab xPlore | Automated Immunoassays | Gyros Protein Technologies Available online: https://www.gyrosproteintechnologies.com/gyrolab-xplore-immunoassay-system (accessed on Feb 5, 2022).

40. Kim, J.; Kido, H.; Rangel, R.H.; Madou, M.J. Passive flow switching valves on a centrifugal microfluidic platform. *Sensors Actuators B Chem.* **2008**, *128*, 613–621, doi:10.1016/J.SNB.2007.07.079.

41. Morijiri, T.; Sunahiro, S.; Senaha, M.; Yamada, M.; Seki, M. Sedimentation pinched-flow fractionation for size- and density-based particle sorting in microchannels. *Microfluid. Nanofluidics* **2011**, *11*, 105–110, doi:10.1007/s10404-011-0785-6.

42. Bauer, M.; Ataei, M.; Caicedo, M.; Jackson, K.; Madou, M.; Bousse, L. Burst valves for commercial microfluidics: a critical analysis. *Microfluid. Nanofluidics* **2019**, *23*, 1–12, doi:10.1007/s10404-019-2252-8.

43. Ducrée, J.; Haeberle, S.; Lutz, S.; Pausch, S.; Von Stetten, F.; Zengerle, R. The centrifugal microfluidic Bio-Disk platform. *J. Micromechanics Microengineering* **2007**, *17*, S103, doi:10.1088/0960-1317/17/7/S07.

44. Vesel, A.; Mozetic, M. Surface modification and ageing of PMMA polymer by oxygen plasma treatment. *Vacuum* **2012**, *86*, 634–637, doi:10.1016/J.VACUUM.2011.07.005.

45. Gorkin, R.; Park, J.; Siegrist, J.; Amasia, M.; Lee, B.S.; Park, J.M.; Kim, J.; Kim, H.; Madou, M.; Cho, Y.K. Centrifugal microfluidics for biomedical applications. *Lab Chip* **2010**, *10*, 1758–1773, doi:10.1039/b924109d.

46. Gorkin, R.; Clime, L.; Madou, M.; Kido, H. Pneumatic pumping in centrifugal microfluidic platforms. *Microfluid. Nanofluidics* **2010**, *9*, 541–549, doi:10.1007/s10404-010-0571-x.

47. Schwemmer, F.; Zehnle, S.; Mark, D.; Von Stetten, F.; Zengerle, R.; Paust, N. A microfluidic timer for timed valving and pumping in centrifugal microfluidics. *Lab Chip* **2015**, *15*, 1545–1553, doi:10.1039/c4lc01269k.

48. Abi-Samra, K.; Hanson, R.; Madou, M.; Gorkin, R.A. Infrared controlled waxes for liquid handling and storage on a CD-microfluidic platform. *Lab Chip* **2011**, *11*, 723–726, doi:10.1039/C0LC00160K.

49. Park, J.M.; Cho, Y.K.; Lee, B.S.; Lee, J.G.; Ko, C. Multifunctional microvalves control by optical illumination on nanoheaters and its application in centrifugal microfluidic devices. *Lab Chip* **2007**, *7*, 557–564, doi:10.1039/B616112J.

50. Kim, T.H.; Sunkara, V.; Park, J.; Kim, C.J.; Woo, H.K.; Cho, Y.K. A lab-on-a-disc with reversible and thermally stable diaphragm valves. *Lab Chip* **2016**, *16*, 3741–3749, doi:10.1039/c6lc00629a.

51. Aeinehvand, M.M.; Weber, L.; Jiménez, M.; Palermo, A.; Bauer, M.; Loeffler, F.F.; Ibrahim, F.; Breitling, F.; Korvink, J.; Madou, M.; et al. Elastic reversible valves on centrifugal microfluidic platforms. *Lab Chip* **2019**, *19*, 1090–1100, doi:10.1039/C8LC00849C.

52. Gorkin, R.; Nwankire, C.E.; Gaughran, J.; Zhang, X.; Donohoe, G.G.; Rook, M.; O'Kennedy, R.; Ducrée, J. Centrifugo-pneumatic valving utilizing dissolvable films. *Lab Chip* **2012**, *12*, 2894–2902, doi:10.1039/C2LC20973J.

53. Abi-Samra, K.; Clime, L.; Kong, L.; Gorkin, R.; Kim, T.H.; Cho, Y.K.; Madou, M. Thermo-pneumatic pumping in centrifugal microfluidic platforms. *Microfluid. Nanofluidics* **2011**, *11*, 643–652, doi:10.1007/s10404-011-0830-5.

54. Kong, M.C.R.; Salin, E.D. Pneumatically pumping fluids radially inward on centrifugal microfluidic platforms in motion. *Anal. Chem.* **2010**, *82*, 8039–8041, doi:10.1021/ac102071b.

55. Cai, Z.; Xiang, J.; Zhang, B.; Wang, W. A magnetically actuated valve for centrifugal microfluidic applications. *Sensors Actuators, B Chem.* **2015**, *206*, 22–29, doi:10.1016/j.snb.2014.08.087.

56. Romero-Soto, F.O.; Aeinehvand, M.M.; Martinez-Chapa, S.O. Wirelessly-controlled

electrolysis pumps on lab-on-a-disc for automation of bioanalytical assays. *Mater. Today Proc.* **2020**, doi:10.1016/j.matpr.2020.10.041.

57. Clime, L.; Brassard, D.; Geissler, M.; Veres, T. Active pneumatic control of centrifugal microfluidic flows for lab-on-a-chip applications. *Lab Chip* **2015**, *15*, 2400–2411, doi:10.1039/c4lc01490a.

58. Noroozi, Z.; Kido, H.; Madou, M.J. Electrolysis-Induced Pneumatic Pressure for Control of Liquids in a Centrifugal System. *J. Electrochem. Soc.* **2011**, *158*, P130, doi:10.1149/2.028111jes.

59. Garcia-Cordero, J.L.; Basabe-Desmonts, L.; Ducrée, J.; Ricco, A.J. Liquid recirculation in microfluidic channels by the interplay of capillary and centrifugal forces. *Microfluid. Nanofluidics* **2010**, *9*, 695–703, doi:10.1007/s10404-010-0585-4.

60. Pishbin, E.; Eghbal, M.; Fakhari, S.; Kazemzadeh, A.; Navidbakhsh, M. The effect of moment of inertia on the liquids in centrifugal microfluidics. *Micromachines* **2016**, *7*, 1–12, doi:10.3390/mi7120215.

61. Kong, M.C.R.; Bouchard, A.P.; Salin, E.D. Displacement pumping of liquids radially inward on centrifugal microfluidic platforms in motion. *Micromachines* **2012**, *3*, 1–9, doi:10.3390/mi3010001.

62. Soroori, S.; Rodriguez-Delgado, J.M.; Kido, H.; Dieck-Assad, G.; Madou, M.; Kulinsky, L. The use of polybutene for controlling the flow of liquids in centrifugal microfluidic systems. *Microfluid. Nanofluidics* **2016**, *20*, 1–13, doi:10.1007/s10404-015-1677-y.

63. Zehnle, S.; Schwemmer, F.; Roth, G.; Von Stetten, F.; Zengerle, R.; Paust, N. Centrifugo-dynamic inward pumping of liquids on a centrifugal microfluidic platform. *Lab Chip* **2012**, *12*, 5142–5145, doi:10.1039/c2lc40942a.

64. Godino, N.; Gorkin, R.; Linares, A. V.; Burger, R.; Ducrée, J. Comprehensive integration of homogeneous bioassays via centrifugo-pneumatic cascading. *Lab Chip* **2013**, *13*, 685–694, doi:10.1039/c2lc40722a.

65. Aeinehvand, M.M.; Ibrahim, F.; Harun, S.W.; Al-Faqheri, W.; Thio, T.H.G.; Kazemzadeh, A.; Madou, M. Latex micro-balloon pumping in centrifugal microfluidic platforms. *Lab Chip* **2014**, *14*, 988–997, doi:10.1039/c3lc51116b.

66. Aeinehvand, M.M.; Ibrahim, F.; Harun, S.W.; Djordjevic, I.; Hosseini, S.; Rothan, H.A.; Yusof, R.; Madou, M.J. Biosensing enhancement of dengue virus using microballoon mixers on centrifugal microfluidic platforms. *Biosens. Bioelectron.* **2015**, *67*, 424–430, doi:10.1016/j.bios.2014.08.076.

67. Groisman, A.; Steinberg, V. Efficient mixing at low Reynolds numbers using polymer additives. *Nat. 2001 4106831* **2001**, *410*, 905–908, doi:10.1038/35073524.

68. La, M.; Park, S.J.; Kim, H.W.; Park, J.J.; Ahn, K.T.; Ryew, S.M.; Kim, D.S. A centrifugal force-based serpentine micromixer (CSM) on a plastic lab-on-A-disk for biochemical assays. *Microfluid. Nanofluidics* **2013**, *15*, 87–98, doi:10.1007/S10404-012-1127-Z/FIGURES/15.

69. Kuo, J.N.; Li, B.S. Lab-on-CD microfluidic platform for rapid separation and mixing of

plasma from whole blood. *Biomed. Microdevices* **2014**, *16*, 549–558, doi:10.1007/S10544-014-9857-1/FIGURES/6.

70. Hin, S.; Paust, N.; Keller, M.; Rombach, M.; Strohmeier, O.; Zengerle, R.; Mitsakakis, K. Temperature change rate actuated bubble mixing for homogeneous rehydration of dry pre-stored reagents in centrifugal microfluidics. *Lab Chip* **2018**, *18*, 362–370, doi:10.1039/c7lc01249g.

71. Burger, S.; Schulz, M.; Von Stetten, F.; Zengerle, R.; Paust, N. Rigorous buoyancy driven bubble mixing for centrifugal microfluidics. *Lab Chip* **2016**, *16*, 261–268, doi:10.1039/C5LC01280E.

72. Noroozi, Z.; Kido, H.; Micic, M.; Pan, H.; Bartolome, C.; Princevac, M.; Zoval, J.; Madou, M. Reciprocating flow-based centrifugal microfluidics mixer. *Rev. Sci. Instrum.* **2009**, *80*.

73. Noroozi, Z.; Kido, H.; Peytavi, R.; Nakajima-Sasaki, R.; Jasinskas, A.; Micic, M.; Felgner, P.L.; Madou, M.J. A multiplexed immunoassay system based upon reciprocating centrifugal microfluidics. *Rev. Sci. Instrum.* **2011**, *82*, doi:10.1063/1.3597578.

74. Riegger, L.; Zengerle, R.; Ducrée, J.; Grumann, M.; Geipel, A.; Riegger, L. Magneto-hydrodynamic micromixing for centrifugal lab-on-a-disk platforms. *Spec. Publ. Soc. Chem.* **2004**, 593–595.

75. Kido, H.; Micic, M.; Smith, D.; Zoval, J.; Norton, J.; Madou, M. A novel, compact disk-like centrifugal microfluidics system for cell lysis and sample homogenization. *Colloids*

Surfaces B Biointerfaces **2007**, *58*, 44–51, doi:10.1016/j.colsurfb.2007.03.015.

76. Haeberle, S.; Brenner, T.; Zengerle, R.; Ducrée, J. Centrifugal extraction of plasma from whole blood on a rotating disk. *Lab Chip* **2006**, *6*, 776–781, doi:10.1039/B604145K.

77. Amasia, M.; Madou, M. Large-volume centrifugal microfluidic device for blood plasma separation. *Bioanalysis* **2010**, *2*, 1701–1710, doi:10.4155/bio.10.140.

78. Kim, N.; Dempsey, C.M.; Zoval, J. V.; Sze, J.Y.; Madou, M.J. Automated microfluidic compact disc (CD) cultivation system of Caenorhabditis elegans. *Sensors Actuators, B Chem.* **2007**, *122*, 511–518, doi:10.1016/j.snb.2006.06.026.

79. Ren, Y.; Chow, L.M.C.; Leung, W.W.F. Cell culture using centrifugal microfluidic platform with demonstration on Pichia pastoris. *Biomed. Microdevices* **2013**, *15*, 321–337, doi:10.1007/s10544-012-9735-7.

80. Perebikovsky, A.; Liu, Y.; Hwu, A.; Kido, H.; Shamloo, E.; Song, D.; Monti, G.; Shoval, O.; Gussin, D.; Madou, M. Rapid sample preparation for detection of antibiotic resistance on a microfluidic disc platform. *Lab Chip* **2021**, *21*, 534–545, doi:10.1039/d0lc00838a.

81. Geissler, M.; Brassard, D.; Clime, L.; Pilar, A.V.C.; Malic, L.; Daoud, J.; Barrère, V.; Luebbert, C.; Blais, B.W.; Corneau, N.; et al. Centrifugal microfluidic lab-on-a-chip system with automated sample lysis, DNA amplification and microarray hybridization for identification of enterohemorrhagic: Escherichia coli culture

isolates. *Analyst* **2020**, *145*, 6831–6845, doi:10.1039/d0an01232g.

82. Nestorova, G.G.; Hasenstein, K.; Nguyen, N.; DeCoster, M.A.; Crews, N.D. Lab-on-a-chip mRNA purification and reverse transcription via a solid-phase gene extraction technique. *Lab Chip* **2017**, *17*, 1128–1136, doi:10.1039/c6lc01421f.

83. Hwang, S.H.; Kim, D.E.; Im, J.H.; Kang, S.J.; Lee, D.H.; Son, S.J. Rapid visual identification of PCR amplified nucleic acids by centrifugal gel separation: Potential use for molecular point-of-care tests. *Biosens. Bioelectron.* **2016**, *79*, 829–834, doi:10.1016/j.bios.2016.01.006.

84. Amasia, M.; Cozzens, M.; Madou, M.J. Centrifugal microfluidic platform for rapid PCR amplification using integrated thermoelectric heating and ice-valving. *Sensors Actuators, B Chem.* **2012**, *161*, 1191–1197, doi:10.1016/j.snb.2011.11.080.

85. Oh, S.J.; Park, B.H.; Choi, G.; Seo, J.H.; Jung, J.H.; Choi, J.S.; Kim, D.H.; Seo, T.S. Fully automated and colorimetric foodborne pathogen detection on an integrated centrifugal microfluidic device. *Lab Chip* **2016**, *16*, 1917–1926, doi:10.1039/c6lc00326e.

86. Rombach, M.; Hin, S.; Specht, M.; Johannsen, B.; Lüddecke, J.; Paust, N.; Zengerle, R.; Roux, L.; Sutcliffe, T.; Peham, J.R.; et al. RespiDisk: a point-of-care platform for fully automated detection of respiratory tract infection pathogens in clinical samples. *Analyst* **2020**, *145*, 7040–7047, doi:10.1039/D0AN01226B.

87. Schulz, M.; Calabrese, S.; Hausladen, F.; Wurm, H.; Drossart, D.; Stock, K.; Sobieraj,

A.M.; Eichenseher, F.; Loessner, M.J.; Schmelcher, M.; et al. Point-of-care testing system for digital single cell detection of MRSA directly from nasal swabs. *Lab Chip* **2020**, *20*, 2549–2561, doi:10.1039/D0LC00294A.

88. Peng, H.; Zhu, M.; Gao, Z.; Liao, C.; Jia, C.; Wang, H.; Zhou, H.; Zhao, J. A centrifugal microfluidic emulsifier integrated with oil storage structures for robust digital LAMP. *Biomed. Microdevices* **2020**, *22*, 1–10, doi:10.1007/S10544-020-0475-9/FIGURES/6.

89. Gowda, H.N.; Kido, H.; Wu, X.; Shoval, O.; Lee, A.; Lorenzana, A.; Madou, M.; Hoffmann, M.; Jiang, S.C. Development of a proof-of-concept microfluidic portable pathogen analysis system for water quality monitoring. *Sci. Total Environ.* **2022**, *813*, 152556, doi:10.1016/J.SCITOTENV.2021.152556.

90. Schuler, F.; Schwemmer, F.; Trotter, M.; Wadle, S.; Zengerle, R.; Von Stetten, F.; Paust, N. Centrifugal step emulsification applied for absolute quantification of nucleic acids by digital droplet RPA. *Lab Chip* **2015**, *15*, 2759–2766, doi:10.1039/C5LC00291E.

91. Schuler, F.; Trotter, M.; Geltman, M.; Schwemmer, F.; Wadle, S.; Domínguez-Garrido, E.; López, M.; Cervera-Acedo, C.; Santibáñez, P.; Von Stetten, F.; et al. Digital droplet PCR on disk. *Lab Chip* **2016**, *16*, 208–216, doi:10.1039/c5lc01068c.

92. Lee, B.S.; Lee, J.N.; Park, J.M.; Lee, J.G.; Kim, S.; Cho, Y.K.; Ko, C. A fully automated immunoassay from whole blood on a disc. *Lab Chip* **2009**, *9*, 1548–1555, doi:10.1039/B820321K.

93. Park, J.; Sunkara, V.; Kim, T.H.; Hwang, H.; Cho, Y.K. Lab-on-a-disc for fully integrated

multiplex immunoassays. *Anal. Chem.* **2012**, *84*, 2133–2140, doi:10.1021/AC203163U/SUPPL_FILE/AC203163U_SI_001.AVI.

94. Kim, T.H.; Abi-Samra, K.; Sunkara, V.; Park, D.K.; Amasia, M.; Kim, N.; Kim, J.; Kim, H.; Madou, M.; Cho, Y.K. Flow-enhanced electrochemical immunosensors on centrifugal microfluidic platforms. *Lab Chip* **2013**, *13*, 3747–3754, doi:10.1039/c3lc50374g.

95. Shen, M.; Chen, Y.; Zhu, Y.; Zhao, M.; Xu, Y. Enhancing the Sensitivity of Lateral Flow Immunoassay by Centrifugation-Assisted Flow Control. *Anal. Chem.* **2019**, *91*, 4814–4820, doi:10.1021/acs.analchem.9b00421.

96. Lord-Doubi/MDX_Spin_Local Available online: https://github.com/Lord-Doubi/MDX_Spin_Local (accessed on Feb 6, 2022).

97. Halford, C.; Gonzalez, R.; Campuzano, S.; Hu, B.; Babbitt, J.T.; Liu, J.; Wang, J.; Churchill, B.M.; Haakea, D.A. Rapid antimicrobial susceptibility testing by sensitive detection of precursor rrna using a novel electrochemical biosensing platform. *Antimicrob. Agents Chemother.* **2013**, *57*, 936–943, doi:10.1128/AAC.00615-12.

98. Ward, K.; Fan, Z.H. Mixing in microfluidic devices and enhancement methods. *J. Micromechanics Microengineering* **2015**, *25*, 094001, doi:10.1088/0960-1317/25/9/094001.

99. Meijer, H.E.H.; Singh, M.K.; Kang, T.G.; Den Toonder, J.M.J.; Anderson, P.D. Passive and Active Mixing in Microfluidic Devices. *Macromol. Symp.* **2009**, *279*, 201–209, doi:10.1002/MASY.200950530.

100. Brennan, M.D.; Rexius-Hall, M.L.; Elgass, L.J.; Eddington, D.T. Oxygen control with microfluidics. *Lab Chip* **2014**, *14*, 4305–4318, doi:10.1039/C4LC00853G.

101. Situma, C.; Hashimoto, M.; Soper, S.A. Merging microfluidics with microarray-based bioassays. *Biomol. Eng.* **2006**, *23*, 213–231, doi:10.1016/J.BIOENG.2006.03.002.

102. Heller, M.J. DNA MICROARRAY TECHNOLOGY: Devices, Systems, and Applications. *Annu. Rev. Biomed. Eng* **2002**, *4*, 129–53, doi:10.1146/annurev.bioeng.4.020702.153438.

103. Zhong, Q.; Ding, H.; Gao, B.; He, Z.; Gu, Z. Advances of Microfluidics in Biomedical Engineering. *Adv. Mater. Technol.* **2019**, *4*, 1800663, doi:10.1002/ADMT.201800663.

104. Lukacs, G.L.; Haggie, P.; Seksek, O.; Lechardeur, D.; Freedman, N.; Verkman, A.S. Size-dependent DNA Mobility in Cytoplasm and Nucleus. *J. Biol. Chem.* **2000**, *275*, 1625–1629, doi:10.1074/JBC.275.3.1625.

105. Gosting, L.J. Measurement and Interpretation of Diffusion Coefficients of Proteins. *Adv. Protein Chem.* **1956**, *11*, 429–554, doi:10.1016/S0065-3233(08)60425-8.

106. Wang, L.; Li, P.C.H. Microfluidic DNA microarray analysis: A review. *Anal. Chim. Acta* **2011**, *687*, 12–27, doi:10.1016/J.ACA.2010.11.056.

107. Li, J.; Zrazhevskiy, P.; Gao, X. Eliminating Size-Associated Diffusion Constraints for Rapid On-Surface Bioassays with Nanoparticle Probes. *Small* **2016**, *12*, 1035–1043, doi:10.1002/smll.201503101.

108. Burger, R.; Reis, N.; Da Fonseca, J.G.; Ducrée, J. Plasma extraction by centrifugo-

pneumatically induced gating of flow. *J. Micromechanics Microengineering* **2013**, *23*, 5, doi:10.1088/0960-1317/23/3/035035.

109. Hohlfelder, R.J. Bulge and Blister Testing of Thin Films and Their Interfaces, Stanford University, 1999.

110. Gad-el-Hak, M. *MEMS: Design and Fabrication*; CRC press, 2021;

111. Siegrist, J.; Amasia, M.; Singh, N.; Banerjee, D.; Madou, M. Numerical modeling and experimental validation of uniform microchamber filling in centrifugal microfluidics. *Lab Chip* **2010**, *10*, 876–886, doi:10.1039/b917880e.

112. Lee, C.Y.; Chang, C.L.; Wang, Y.N.; Fu, L.M. Microfluidic mixing: A review. *Int. J. Mol. Sci.* **2011**, *12*, 3263–3287, doi:10.3390/ijms12053263.

Appendix A: System Development

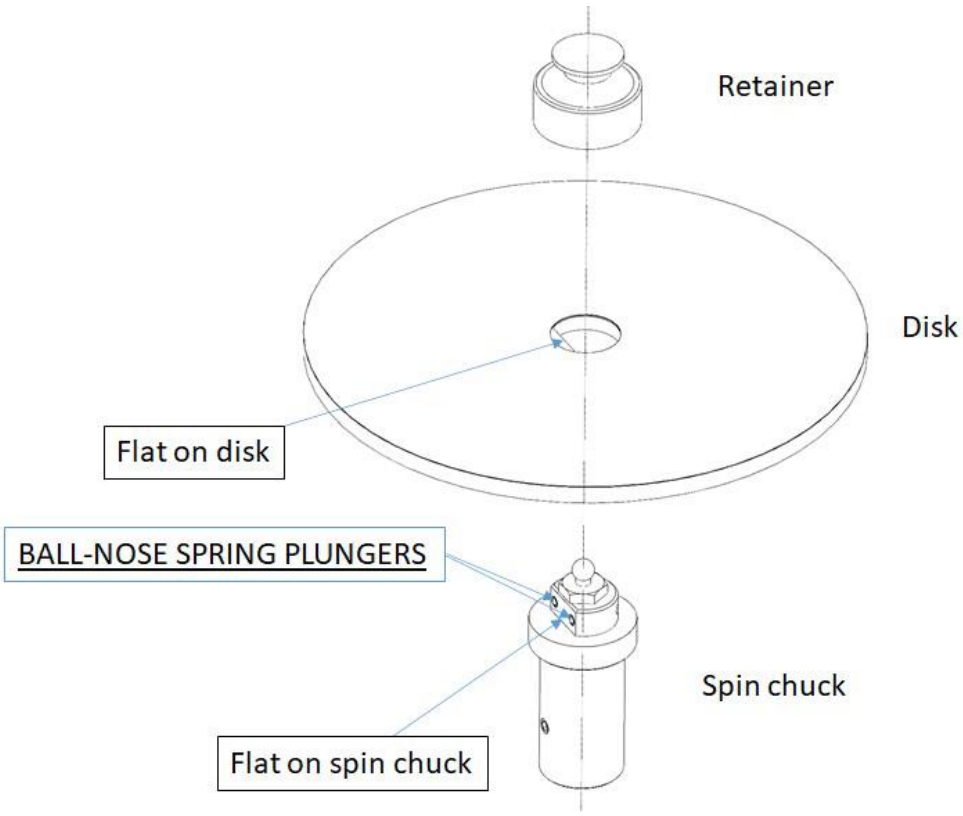

Figure A1. The spinchuck and spring-loaded balls for instrument-cartridge interface.

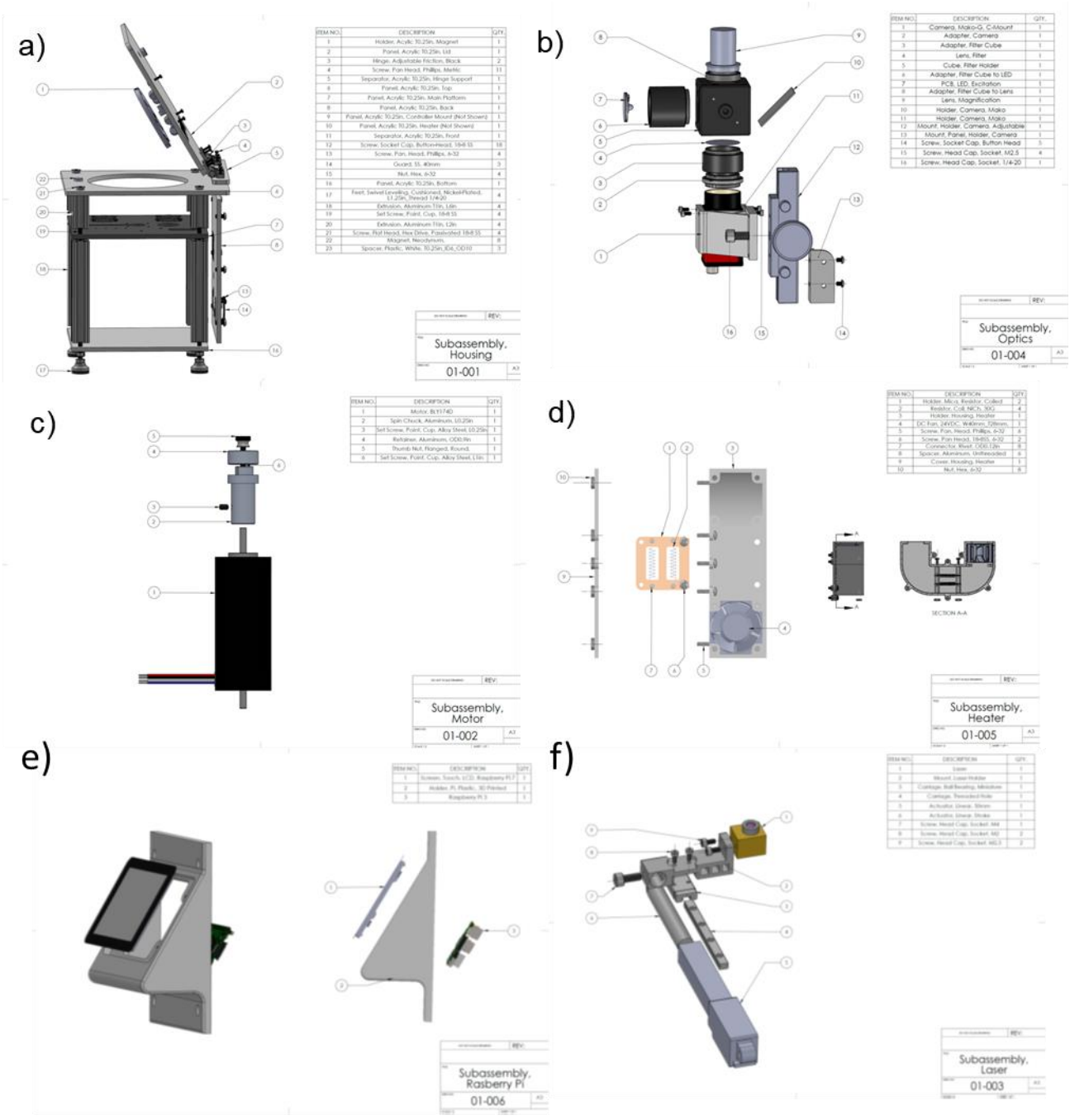

Figure A2. Components of the sub-units. a) enclosure, b) optical unit, c) main motor, d) thermal control unit, e) program control unit, and f) laser valving unit.

Software and programming for SpinBox

The software that controls the machine is based on a Python3 program with a set of libraries including pyqt4 as the graphical user interface. It has the following functions:

1. Controlling the movement of the main, brushless DC motor. This includes spinning at a specified RPM, acceleration/deceleration (RPM/s), oscillation at a specified angle and frequency (Hz), and angular positioning.
2. Controlling the linear actuator to move the laser to a certain radial position. A linear actuator is used here to carry a 5W blue light laser diode. A PWM code is sent from the raspberry pi to the actuator through GPIO pins on the Raspberry Pi. The motor and linear actuator are moved correspondingly to target the laser at specific valving position.
3. Controlling the laser with desired power. The laser is controlled by an PWM code to adjust the power for fast and accurate actuation of the valve.
4. Controlling the excitation led to light up the detection area. A GPIO code is integrated to control a 1W led excitation source for the integrated fluorescent microscope.
5. Controlling the custom-built fluorescent microscope to take picture. Through an ethernet cable, the camera is controlled through Pymba (https://github.com/morefigs/pymba), a python wrapper for Allied Vision's Vimba C API. The library enables control over camera parameters such as exposure and gain.
6. Processing the image with OpenCV code. OpenCV-python is an open-source computer vision library that was used to detect and measure the fluorescence intensity of each probe binding area. Pictures of the detection area before and after hybridization are taken by the custom-built fluorescence microscope camera for comparison. To process

the fluorescent image (a), each image is first background subtracted (b). Then the resulting image is smoothed with a Gaussian blur algorithm. A threshold is applied to remove any spikes from the picture which may be falsely recognized as detection spots (c). Finally, the "findContours" function is used to outline the perimeter of the fluorescent spots and the intensity of each pixel is summed up as the total fluorescence intensity (d).

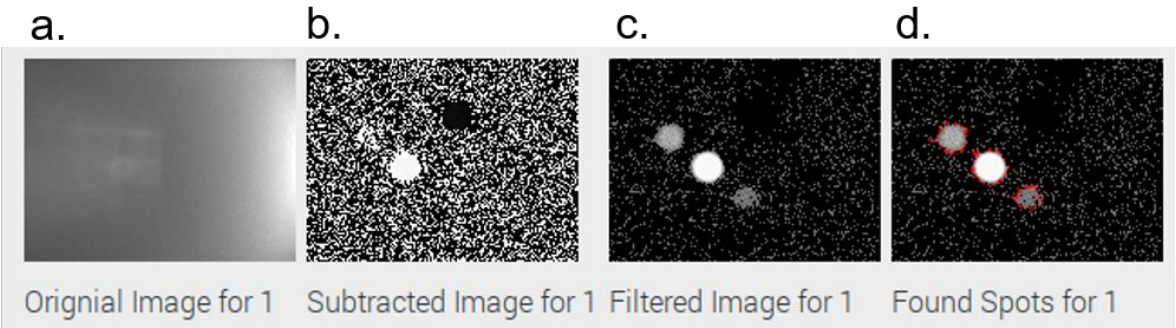

Appendix B: Recirculation Mechanism

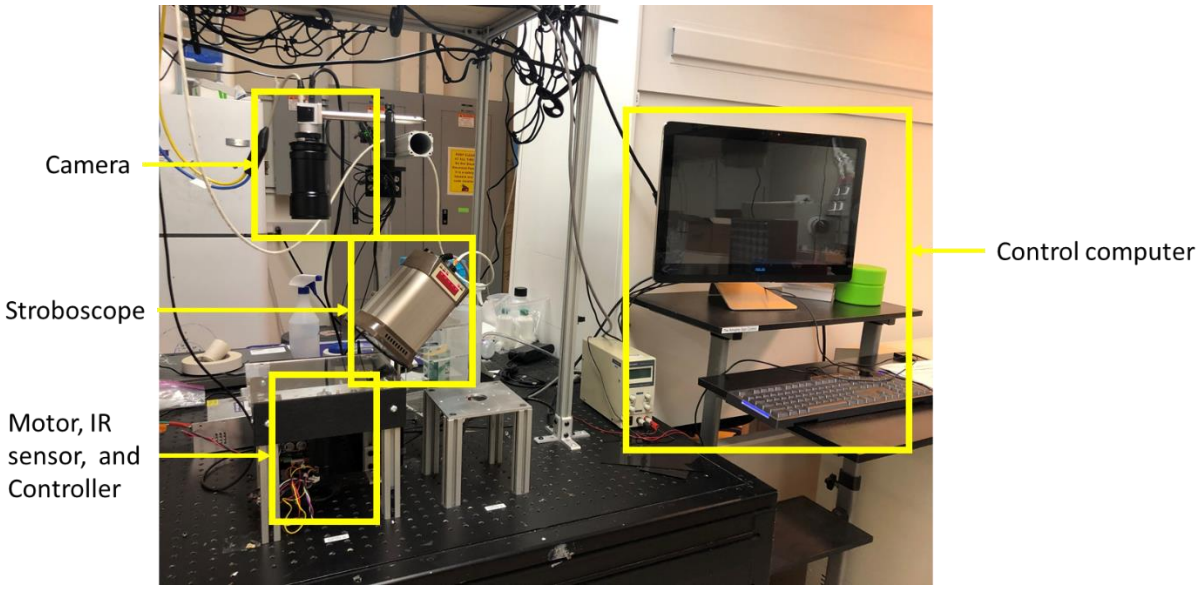

Figure B1. Spinstand used in this research for fluidic observation.

Table B1. Protocol for recirculation/mixing and quantification test

Steps	Protocol for recirculation/mixing and quantification test
Step 1	0-3600 rpm in 3 seconds
Step 2	Stay at 3600 rpm for 7 seconds
Step 3	3600-180 rpm in 1 second
Step 4	Stay at 180 rpm for 4 seconds
Step 5	180-3600 rpm in 3 seconds
Step 6	Stay at 3600 rpm for 2 seconds
Step 7	Repeat from step 3 to step 6 for 3 times
Step 8	3600-0 rpm gradually
Step 9	End test

Table B2. Protocol for blood/plasma separation test

Steps	Protocol for blood/plasma separation test
Step 1	0-4500 rpm in 5 seconds
Step 2	Stay at 4500 rpm for 305 seconds
Step 3	4500-180 rpm in 1 seconds
Step 4	Stay at 180 rpm for 4 seconds

Step 5	180-3600 rpm in 3 seconds
Step 6	Stay at 3600 rpm for 2 seconds
Step 7	3600-180 rpm in 1 second
Step 8	Repeat from step 4 to step 7 for 2 times
Step 9	Stay at 180 rpm for 4 seconds
Step 10	180-3600 rpm in 3 seconds
Step 11	Stay at 3600 rpm for 2 seconds
Step 12	3600-0 rpm gradually
Step 13	End test

Table B3. Cycle protocol for hybridization efficiency test.

Steps of cycles	Reciprocation (2 steps)	Recirculation (3 steps)
Step 1	3600 for 5 seconds	3600 for 2 seconds
Step 2	900 for 5 seconds	180 for 2 seconds
Step 3		900 for 6 seconds

Table B4. Cycle protocol for hybridization efficiency test.

Steps the assay	Reagent	Volume	Time
Step 1	Primary antibodies	50 µl	10 mins (60 cycles)
Step 2	TBST wash buffer	50 µl	10 mins (60 cycles)
Step 3	2nd antibodies	50 µl	10 mins (60 cycles)
Step 4	TBST wash buffer	50 µl	10 mins (60 cycles)

	1	2	3	4	5	6	7	8	9	10
1	Fiducial	Buffer	Buffer	Buffer	Buffer	Buffer	Buffer	Buffer	Buffer	Fiducial
2	SARS-CoV2.RBD.mFc	SARS-CoV2.RBD.mFc	SARS-CoV2.RBD.mFc	SARS-CoV2.RBD.mFc	SARS-CoV2.RBD.mFc	SARS-CoV2.RBD.mFc	SARS-CoV2.RBD.mFc	SARS-CoV2.RBD.mFc	SARS-CoV2.RBD.mFc	SARS-CoV2.RBD.mFc
3	SARS-CoV2.RBD.mFc	SARS-CoV2.RBD.mFc	SARS-CoV2.RBD.mFc	SARS-CoV2.RBD.mFc	SARS-CoV2.RBD.mFc	SARS-CoV2.RBD.mFc	SARS-CoV2.RBD.mFc	SARS-CoV2.RBD.mFc	SARS-CoV2.RBD.mFc	SARS-CoV2.RBD.mFc
4	SARS-CoV2.RBD.mFc	SARS-CoV2.RBD.mFc	SARS-CoV2.RBD.mFc	SARS-CoV2.RBD.mFc	SARS-CoV2.RBD.mFc	SARS-CoV2.RBD.mFc	SARS-CoV2.RBD.mFc	SARS-CoV2.RBD.mFc	SARS-CoV2.RBD.mFc	SARS-CoV2.RBD.mFc
5	SARS-CoV2.RBD.mFc	SARS-CoV2.RBD.mFc	SARS-CoV2.RBD.mFc	SARS-CoV2.RBD.mFc	SARS-CoV2.RBD.mFc	SARS-CoV2.RBD.mFc	SARS-CoV2.RBD.mFc	SARS-CoV2.RBD.mFc	SARS-CoV2.RBD.mFc	SARS-CoV2.RBD.mFc
6	SARS-CoV2.RBD.mFc	SARS-CoV2.RBD.mFc	SARS-CoV2.RBD.mFc	SARS-CoV2.RBD.mFc	SARS-CoV2.RBD.mFc	SARS-CoV2.RBD.mFc	SARS-CoV2.RBD.mFc	SARS-CoV2.RBD.mFc	SARS-CoV2.RBD.mFc	SARS-CoV2.RBD.mFc
7	SARS-CoV2.RBD.mFc	SARS-CoV2.RBD.mFc	SARS-CoV2.RBD.mFc	SARS-CoV2.RBD.mFc	SARS-CoV2.RBD.mFc	SARS-CoV2.RBD.mFc	SARS-CoV2.RBD.mFc	SARS-CoV2.RBD.mFc	SARS-CoV2.RBD.mFc	SARS-CoV2.RBD.mFc
8	SARS-CoV2.RBD.mFc	SARS-CoV2.RBD.mFc	SARS-CoV2.RBD.mFc	SARS-CoV2.RBD.mFc	SARS-CoV2.RBD.mFc	SARS-CoV2.RBD.mFc	SARS-CoV2.RBD.mFc	SARS-CoV2.RBD.mFc	SARS-CoV2.RBD.mFc	SARS-CoV2.RBD.mFc
9	SARS-CoV2.RBD.mFc	SARS-CoV2.RBD.mFc	SARS-CoV2.RBD.mFc	SARS-CoV2.RBD.mFc	SARS-CoV2.RBD.mFc	SARS-CoV2.RBD.mFc	SARS-CoV2.RBD.mFc	SARS-CoV2.RBD.mFc	SARS-CoV2.RBD.mFc	SARS-CoV2.RBD.mFc
10	Fiducial	HuIgG_0.5	HuIgG_0.5	SARS-CoV2.RBD.mFc	SARS-CoV2.RBD.mFc	SARS-CoV2.RBD.mFc	SARS-CoV2.RBD.mFc	a.HuIgG_0.5	a.HuIgG_0.5	Buffer

Figure B2. Layout of the microarray used in hybridization tests.

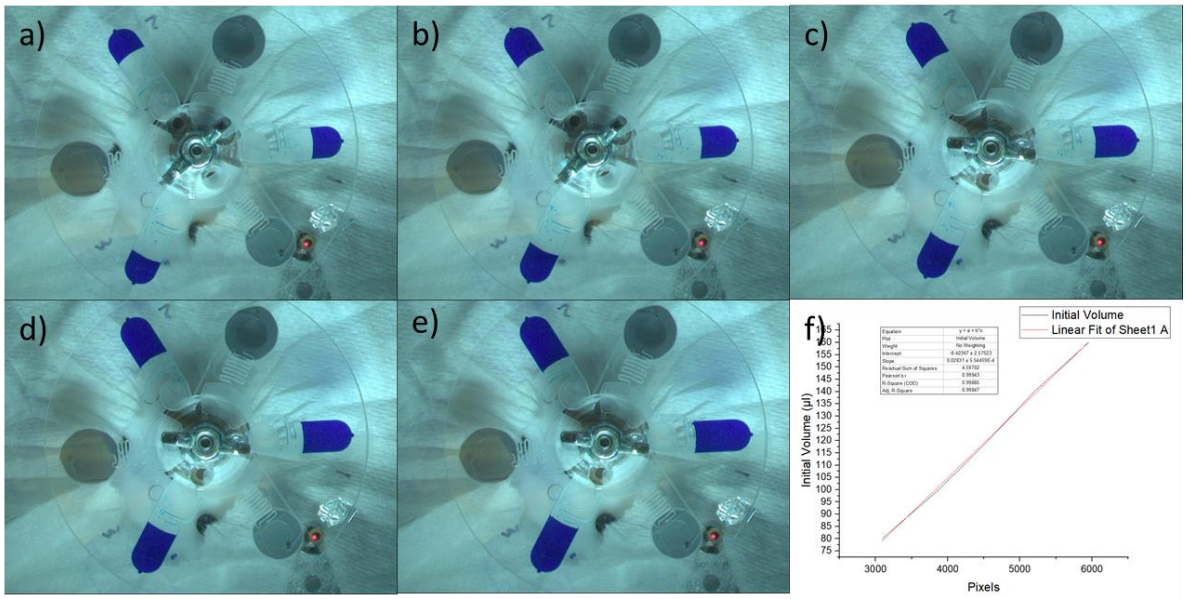

Figure B3. Calibration images of inward pumping efficiency tests. a)-e) represent volume of 80µl, 100µl, 120µl, 140µl, and 160µl respectively. f) is the linear fitting of the pixels and volume.

Table B5. Parameters used for volume calculation.

Parameters	Value	Parameters	Value
C_1	8/3	θ_p	68°
C_2	2	σ	40 mj/m^2
r_1	11.5 mm	l	0.5 mm
r_2	29 mm	ρ	10^3 kg/m^3
a	$3, 4, and\ 5$ mm	ω	$6\pi/s$
d	100μm	t	100 μm
θ_a	110.5°	β	90°
σ_0	0 MPa	$L\ when\ a = 3$	34.04 mm
E	0.135 MPa	$L\ when\ a = 4$	34.88 mm
ν	0.48	$L\ when\ a = 5$	35.84 mm

Calculation of Reynolds number for mixing

As a typical indicator to characterize the fluidic behavior, Reynolds number Re_D was introduced here to investigate the flow in the recirculating chamber, which can be described using the following equation:

$$Re = \frac{QD}{\nu A},$$

where the kinetic viscosity ν of water with a value of $1.004 \times 10^{-6}\ m^2/s$. Q is the volumetric velocity of liquid entering the chamber, which was $2.5 \times 10^{-7}\ m^3/s$ calculated from the video. D is the characteristic length of the flow region, which can be described as:

$$D = \frac{4A}{P}$$

where A is the cross-sectional area of the flow, and P is the wetted perimeter. To perform a conservative calculation, a spherical cap was used to represent the inflated recirculating chamber, which is close to the real situation as shown in figure s3. Therefore, the height of the chamber h can be calculated using the equation:

$$V = \frac{1}{6}\pi h(3a^2 + h^2),$$

where V is the volume of the liquid $100\ \mu l$. a is the radius of the recirculating chamber $4\ mm$. Therefore, we have $P = 18.96\ mm$. By substitute in the value for each number, the Reynolds number was calculated to be 52.63 for water that flows in a channel with a circular segment as the shape of the cross-section.

Appendix C: Protocols for AST

Table C1 Assay steps and duration of rRNA based antibiotic susceptibility test.

Step number	Assay step	Duration
1	Incubation	90 mins
2	Lysis	6 mins
3	Neutralization	5 mins
4	Hybridization with detection probe	10 mins
5	Hybridization with capture probe	10 mins
6	1st wash	10 mins
7	2nd wash	10 mins
8	Detection	5 mins

Table C2 Assay steps and duration of rRNA based antibiotic susceptibility test.

Assay step	Protocol	Details
Incubation	Oscillation	2 Hz, 180°
Valve 1	Laser + Spin	2000 RPM
Cell Lysis	Spin	200 RPM
Valve 2	Laser + Spin	2000 RPM
Neutralization	Oscillation	2 Hz, 180°
Valve 3	Laser + Spin	2000 RPM
Hybridization	Oscillation	2 Hz, 180°
Valve 4	Laser + Spin	4000 RPM
Wash 1	Spin	1000 RPM
Wash 2	Spin	1000 RPM
Detection	Position + Camera	0 rpm